Journal of Computational Physics 228 (2009) 952–975

Contents lists available at ScienceDirect

Journal of Computational Physics

journal homepage: www.elsevier.com/locate/jcp

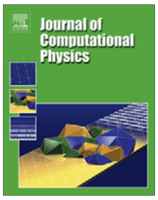

An unsplit staggered mesh scheme for multidimensional magnetohydrodynamics

Dongwook Lee [a], Anil E. Deane [b,*]

[a] ASC FLASH Center, University of Chicago, 5640 S. Ellis, Chicago, IL 60637, United States
[b] Institute for Physical Science and Technology, University of Maryland, College Park, MD 20742, United States

ARTICLE INFO

Article history:
Received 3 December 2007
Received in revised form 18 July 2008
Accepted 20 August 2008
Available online 12 September 2008

Keywords:
MHD
Magnetohydrodynamics
Constrained transport
Corner transport upwind
Unsplit scheme
Staggered mesh
High-order Godunov method

ABSTRACT

We introduce an unsplit staggered mesh scheme (USM) for multidimensional magnetohydrodynamics (MHD) that uses a constrained transport (CT) method with high-order Godunov fluxes and incorporates a new data reconstruction–evolution algorithm for second-order MHD interface states. In this new algorithm, the USM scheme includes so-called "multidimensional MHD terms", proportional to $\nabla \cdot \mathbf{B}$, in a dimensionally-unsplit way in a single update. This data reconstruction–evolution step, extended from the corner transport upwind (CTU) approach of Colella, maintains in-plane dynamics very well, as shown by the advection of a very weak magnetic field loop in 2D. This data reconstruction–evolution algorithm is also of advantage in its consistency and simplicity when extended to 3D. The scheme maintains the $\nabla \cdot \mathbf{B} = 0$ constraint by solving a set of discrete induction equations using the standard CT approach, where the accuracy of the computed electric field directly influences the quality of the magnetic field solution. We address the lack of proper dissipative behavior in the simple electric field averaging scheme and present a new modified electric field construction (MEC) that includes multidimensional derivative information and enhances solution accuracy. A series of comparison studies demonstrates the excellent performance of the full USM–MEC scheme for many stringent multidimensional MHD test problems chosen from the literature. The scheme is implemented and currently freely available in the University of Chicago ASC FLASH Center's FLASH3 release.

1. Introduction

The high-order Godunov method, with its accuracy and robustness, has led to numerous developments in numerical magnetohydrodynamics (MHD). A brief list of these contributions stemming from the use of this method includes the work of Brio and Wu [7], Zachary et al. [43], Dai and Woodward [10], Ryu and Jones [34], Balsara and Spicer [2], Powell et al. [32], Londrillo and Del Zanna [26,27], Pen et al. [30], Balsara [4], Crockett et al. [9], and Gardiner and Stone [16–18].

A number of these studies have highlighted the advantages of using an unsplit formulation in numerical MHD [9,16–18]. The need for having an unsplit MHD formulation arises because dimensional-splitting methods do not include the evolution of the normal (to the sweep direction) magnetic field during each sweep. An early effort to find an alternative formulation to overcome this difficulty using conservative schemes can be found in the 8-wave formulation by Powell et al. [32] which explicitly carries the divergence "field".

A recent unsplit MHD scheme for multidimensions by Gardiner and Stone [16,17] identified multidimensional MHD terms that need to be included in unsplit schemes as well as the proper way to include these terms in their algorithm – a

---

* Corresponding author.
E-mail addresses: dongwook@flash.uchicago.edu (D. Lee), deane@ipst.umd.edu (A.E. Deane).

0021-9991/$ - see front matter © 2008 Elsevier Inc. All rights reserved.
doi:10.1016/j.jcp.2008.08.026

combination of constrained transport (CT) and corner transport upwind (CTU) schemes. Even following these key ideas there is still some difficulty in designing an unsplit method to account for all important physics as well its effectiveness, particularly with regard to high-order solution accuracy with the correct physics, robustness, and the algorithm's extensions to 3D.

The present paper addresses these issues in a new unsplit formalism for multidimensional MHD. We present a new data reconstruction–evolution algorithm that yields second-order accurate MHD interface states, and accounts for all necessary multidimensional MHD terms. It should be noted that this data reconstruction–evolution algorithm, as presented for 2D, extends straightforwardly to 3D, unlike [16,17] where additional complexity is introduced [17,18]. Additionally there, the primary 3D integrator, termed 6-solve CTU + CT algorithm, is subject to a reduced CFL stability range, e.g., less than 0.5. In short, the present unsplit staggered mesh (USM) scheme achieves a numerically efficient and consistent MHD algorithm in multidimensions without additional complexity, while maintaining a wide CFL stability range, e.g., less than 1.0.

We begin by briefly reviewing previous relevant work in numerical MHD in the following subsections based on choices of where to collocate magnetic field variables and how to solve the associated $\nabla \cdot \mathbf{B} = 0$ constraint numerically.

1.1. Cell-centered fields algorithms in high-order Godunov MHD

The high-order Godunov method, first developed by van Leer [41] for Euler flows opened a new era of robust and accurate performance in numerical simulations of MHD as well as hydrodynamics. Early efforts in high-order Godunov MHD schemes focused entirely on numerical formulations that collocated the magnetic fields at cell centers because the underlying aspects of Godunov algorithms are based on conservation laws in which the cell-centered variables are conserved. Thus the MHD equations were treated as a straightforward system of conservation laws in earlier Godunov formulations.

In formulations with cell-centered fields there is no particular difficulty encountered except in multidimensions. This is because in 1D MHD the normal field is held constant and divergence-less evolution of the magnetic fields is obtained naturally. In multidimensional MHD, however, the requirement of maintaining the solenoidal constraint involves solving the induction equation, which for ideal MHD has the form,

$$\frac{\partial \mathbf{B}}{\partial t} + \nabla \times \mathbf{E} = 0. \tag{1}$$

Taking the divergence of the induction equation (1) gives

$$\frac{\partial \nabla \cdot \mathbf{B}}{\partial t} = \nabla \cdot (-\nabla \times \mathbf{E}) = 0 \tag{2}$$

and we see that the induction equation implies the divergence-less evolution of the magnetic fields. This analytical result may not hold true numerically, because the discrete divergence of the discrete curl may not give zero identically.

Until recently, two traditional approaches have been proposed to enforce the divergence-free constraint in formulations using cell-centered fields. The first is the projection method, early works in [1,34,43] and recently in [9], which takes a divergence-cleaning step in their high-order Godunov based MHD scheme. In this approach two choices are available, a scalar or vector divergence-cleaning, depending on the choice of real or Fourier spaces in which the divergence-cleaning is performed. The disadvantage of the approach is the cost of the associated Poisson equation solution either by direct or iterative methods.

The second method, the so-called 8-wave formalism, proposed by Powell et al. [32], utilizes the modified MHD equations that explicitly includes source terms proportional to $\nabla \cdot \mathbf{B}$. An additional eighth wave reflects the propagation of the magnetic monopole "field", designed to be convected with local flow speeds, and eventually advected out of the computational domain or otherwise accumulated benignly. Although the scheme is found to be robust and accurate (as compared to the basic conservative scheme), this approach results in a non-conservative form of the MHD governing equations and is susceptible to producing incorrect jump conditions and propagation speeds across discontinuities in certain problems [32,40]. There have also been other approaches [12,20] to extend the 8-wave scheme that manifest $\nabla \cdot \mathbf{B}$ as a source term.

1.2. Cell face-centered fields algorithms in high-order Godunov MHD: the staggered mesh algorithm

To overcome the issues raised in formulating high-order Godunov based MHD using cell-centered fields, researchers have developed various staggered mesh algorithms that use a staggered collocation of the magnetic fields and solve the induction equation (1) via a discrete form of Stokes' theorem.

The staggered mesh algorithm, first introduced by Yee [42] to compute divergence-free MHD flows in a finite difference formulation that transports the electromagnetic fields, has resulted in numerous approaches. Brecht et al. [6] used a staggered mesh formulation for their global MHD modeling of Earth's magnetosphere for which they used a non-linear FCT flux limiter. Evans and Hawley [14] followed a vector potential approach on a staggered grid for evolution of the MHD induction equation. Another approach by DeVore [13] also used the staggered mesh arrangement and applied it using a flux corrected transport (FCT) algorithm. Following Evans and Hawley [14], the term *constrained transport* (CT) has become popular and encompasses all the various methods developed with a staggered mesh approach [2,4,5,11,13,14,16,17,21,22,26,35,40]. The original CT method placed the surface variables – the components of the magnetic field – at the cell face centers (cell faces), and the rest of the volumetric variables such as mass, momentum and energy at the cell centers on a staggered grid. A variant CT approach by Tóth [40] placed all of the variables at the cell centers and used central differencing for the induction equation. Tóth also made an extensive comparison study of different MHD schemes focusing on the divergence-free property of each scheme. He compared various approaches differing in how the base scheme (e.g., van Leer's TVD-MUSCL, or Yee's TVD-Lax Friedrichs) is modified with regard to the induction equation. Tóth's study [40] compared not only the three major algorithms (i.e., the projection scheme, 8-wave scheme, and CT-based staggered mesh scheme) but also different approaches within the CT formulations.

In CT schemes, different approaches are adopted in obtaining the electric field, $\mathbf{E} = -\mathbf{u} \times \mathbf{B}$ (in ideal MHD). The *flux*-CT scheme of Balsara and Spicer [2] uses second-order Godunov fluxes to construct $\mathbf{E}$ by using the so-called duality relation between the components of the flux vector and the electric fields. The *field-interpolated* CT scheme of Dai and Woodward [11] uses interpolated magnetic and velocity fields to obtain the electric field in their Godunov-type formulation. Ryu et al. [35] also proposed a *transport-flux-interpolated* CT scheme which basically transports the upwind fluxes along with the upwind correction terms for maintaining the TVD property. Balsara studied a new reconstruction algorithm [3,4] for cell-centered magnetic fields. In this *modified*-CT approach the magnetic fields at each cell center are reconstructed directly from divergence-free cell face field components using a reconstruction polynomial. By design, such reconstructed magnetic fields at the cell centers (and not only the cell face fields) are also guaranteed to maintain the divergence-free constraint. Recently, Gardiner and Stone [16] have developed a multidimensional CT scheme that is consistent with plane–parallel, grid-aligned 1D base flows by modifying the simple arithmetic electric field averaging scheme of Balsara and Spicer [2].

Another approach, the *upwinding*-CT (UTC) scheme, was proposed by Londrillo and Del Zanna [27]. Their approach used a similar reconstruction algorithm as in [3,4] for the magnetic field and evaluates the electric field based on an upwinding strategy in their Godunov-type scheme. In the UTC scheme, the divergence-free property is maintained intrinsically. Yet it is evident from their test results that the scheme suffers from keeping $\nabla \cdot \mathbf{B}$ only approximately low, allowing values up to an order of 10^{-4} (see [26]), while, as shown later, our scheme presented here preserves $\nabla \cdot \mathbf{B}$ to the order of 10^{-12} to 10^{-16} in simulations. It is worth mentioning that, in Tóth's comparative study [40], one of the most accurate high-order MHD schemes is the flux-CT scheme of Balsara and Spicer [2]. Balsara [3,4] has also extended his original flux-CT scheme and implemented it on an AMR grid. As a variant of the central scheme [25], most recently, Li [23] extended the scheme that uses overlapping cells for MHD flows. He also proposed a third-order divergence-free reconstruction and a corresponding third-order CT scheme, giving a third-order accurate algorithm.

In developing our scheme we adopt the flux-CT approach of Balsara and Spicer [2] and extend its basic ideas to develop a new unsplit staggered mesh (USM) scheme. Upon systematically developing a new data reconstruction–evolution algorithm and a new modified electric field construction (MEC) we term our complete scheme USM–MEC.

The paper is organized as follows. In Section 2, we first introduce a new second-order MUSCL-Hancock type data reconstruction–evolution scheme using a single step characteristic decomposition formalism. This step includes multidimensional MHD terms that are important in nonlinear evolutionary plasma flows and updates cell interface states by a half time step. The normal magnetic fields are evolved separately by a half time step, maintaining the divergence-free constraint as well as the continuity restriction across cell interfaces. The data reconstruction–evolution step is followed by solving a Riemann problem that produces high-order Godunov fluxes. Using these fluxes, in Section 3, we present a new modified electric field construction (MEC) algorithm that extends the basic construction scheme of Balsara and Spicer [2] to a scheme containing multidimensional gradient information. We summarize our overall USM–MEC scheme in Section 4. In Section 5 we present numerical results of various test problems that demonstrate the significant qualitative and quantitative performance of our scheme. We conclude the paper in Section 6.

2. The USM scheme in ideal MHD

We focus on solving the equations of ideal magnetohydrodynamics (MHD) formulated as hyperbolic system of conservation laws as

$$\frac{\partial \rho}{\partial t} + \nabla \cdot (\rho \mathbf{u}) = 0, \tag{3}$$

$$\frac{\partial \rho \mathbf{u}}{\partial t} + \nabla \cdot (\rho \mathbf{u}\mathbf{u} - \mathbf{B}\mathbf{B}) + \nabla p_{\text{tot}} = 0, \tag{4}$$

$$\frac{\partial \mathbf{B}}{\partial t} + \nabla \cdot (\mathbf{u}\mathbf{B} - \mathbf{B}\mathbf{u}) = 0, \tag{5}$$

$$\frac{\partial E}{\partial t} + \nabla \cdot (\mathbf{u}E + \mathbf{u}p_{\text{tot}} - \mathbf{B}\mathbf{B} \cdot \mathbf{u}) = 0. \tag{6}$$

The above equations represent the continuity, momentum, induction, and energy equations, respectively. The conservative variables include the plasma mass density ρ, momentum $\rho\mathbf{u}$, magnetic field $\mathbf{B}$, and total energy density E. The plasma velocity is $\mathbf{u}$ and its magnitude $U^2 = u^2 + v^2 + w^2$, current density $\mathbf{j} = \nabla \times \mathbf{B}$, total pressure $p_{\text{tot}} = p + B_{\text{p}}$ where $p = (\gamma - 1)(E - \frac{1}{2}\rho U^2 - \frac{1}{2}B^2)$ is the thermal pressure and $B_{\text{p}} = (B_x^2 + B_y^2 + B_z^2)/2$ the magnetic pressure, and γ the ratio of specific heats. In addition, the MHD equations should satisfy the solenoidal constraint $\nabla \cdot \mathbf{B} = 0$, which is implicit in the conservation form. The above equations can be written in a matrix form, e.g., in 2D,

$$\frac{\partial \mathbf{U}}{\partial t}+\frac{\partial \mathbf{F}}{\partial x}+\frac{\partial \mathbf{G}}{\partial y}=0, \tag{7}$$

where **U** contains the eight MHD conservative variables, and **F** and **G** represent corresponding conservative fluxes in x, y directions. The conservative variable vector **U** is

$$\mathbf{U}=(\rho, \rho u, \rho v, \rho w, B_x, B_y, B_z, E)^{\mathrm{T}} \tag{8}$$

and multidimensional fluxes **F** and **G** are

$$\mathbf{F}=\begin{pmatrix} \rho u \\ \rho u^2+p_{\mathrm{tot}}-B_x^2 \\ \rho u v-B_y B_x \\ \rho u w-B_z B_x \\ 0 \\ u B_y-v B_x(=-E_z) \\ u B_z-w B_x(=E_y) \\ (E+p_{\mathrm{tot}})u-B_x(uB_x+vB_y+wB_z) \end{pmatrix}, \quad \mathbf{G}=\begin{pmatrix} \rho v \\ \rho v u-B_x B_y \\ \rho v^2+p_{\mathrm{tot}}-B_y^2 \\ \rho v w-B_z B_y \\ v B_x-u B_y(=E_z) \\ 0 \\ v B_z-w B_y(=-E_x) \\ (E+p_{\mathrm{tot}})v-B_y(uB_x+vB_y+wB_z) \end{pmatrix}. \tag{9}$$

Note that Ohm's law for perfectly conducting plasma, $\mathbf{E}=-\mathbf{u}\times\mathbf{B}$, has been used, where $\mathbf{E}=(E_x, E_y, E_z)^{\mathrm{T}}$ is the electric field.

2.1. Data reconstruction–evolution scheme for the USM

The first step of the USM scheme for multidimensional MHD makes use of a second-order MUSCL-Hancock type TVD algorithm for its data reconstruction–evolution. The data reconstruction–evolution uses cell-centered variables to calculate cell interface values that are required to solve a Riemann problem. In this reconstruction–evolution step, it is important to include terms that reflect the multidimensional character of the MHD equations. These terms have usually been ignored in dimensionally-split type data reconstruction–evolution formulations but have been highlighted by Crockett et al. [9] and Gardiner and Stone [16,17].

In this section we present a new dimensionally-unsplit data reconstruction–evolution algorithm that includes these multidimensional MHD terms. This approach is computationally more efficient than the 1D Godunov based data reconstruction–evolution schemes because it does not involve solving a Riemann problem which arises in the usual transverse predictor step [8,9,16]. Additionally, it is mathematically more consistent with the governing multidimensional MHD equations than the 1D data reconstruction–evolution algorithm used in [9,16].

We begin our discussion by rewriting the conservative form of Eq. (7) in primitive variables $\mathbf{V}=(\rho, u, v, w, B_x, B_y, B_z, p)^{\mathrm{T}}$,

$$\frac{\partial \mathbf{V}}{\partial t}+\mathbf{A}_x\frac{\partial \mathbf{V}}{\partial x}+\mathbf{A}_y\frac{\partial \mathbf{V}}{\partial y}=0, \tag{10}$$

where the well-known matrices $\mathbf{A}_x$ and $\mathbf{A}_y$ are given by

$$\mathbf{A}_x=\begin{pmatrix} u & \rho & 0 & 0 & 0 & 0 & 0 & 0 \\ 0 & u & 0 & 0 & -\frac{B_x}{\rho} & \frac{B_y}{\rho} & \frac{B_z}{\rho} & \frac{1}{\rho} \\ 0 & 0 & u & 0 & -\frac{B_y}{\rho} & -\frac{B_x}{\rho} & 0 & 0 \\ 0 & 0 & 0 & u & -\frac{B_z}{\rho} & 0 & -\frac{B_x}{\rho} & 0 \\ 0 & 0 & 0 & 0 & 0 & 0 & 0 & 0 \\ 0 & B_y & -B_x & 0 & -v & u & 0 & 0 \\ 0 & B_z & 0 & -B_x & -w & 0 & u & 0 \\ 0 & \gamma p & 0 & 0 & -k\mathbf{u}\cdot\mathbf{B} & 0 & 0 & u \end{pmatrix}, \tag{11}$$

$$\mathbf{A}_y=\begin{pmatrix} v & 0 & \rho & 0 & 0 & 0 & 0 & 0 \\ 0 & v & 0 & 0 & -\frac{B_y}{\rho} & -\frac{B_x}{\rho} & 0 & 0 \\ 0 & 0 & v & 0 & \frac{B_x}{\rho} & -\frac{B_y}{\rho} & \frac{B_z}{\rho} & \frac{1}{\rho} \\ 0 & 0 & 0 & v & 0 & -\frac{B_z}{\rho} & -\frac{B_y}{\rho} & 0 \\ 0 & -B_y & B_x & 0 & v & -u & 0 & 0 \\ 0 & 0 & 0 & 0 & 0 & 0 & 0 & 0 \\ 0 & 0 & B_z & -B_y & 0 & -w & v & 0 \\ 0 & 0 & \gamma p & 0 & 0 & -k\mathbf{u}\cdot\mathbf{B} & 0 & v, \end{pmatrix} \tag{12}$$

with $k = 1 - \gamma$. Note that, from relations (9), there are seven non-trivial equations and one trivial equation for which the time derivatives become zero, yielding the zeros located in each corresponding row in the above 8×8 matrices (11) and (12). In general, assuming the left ($\mathbf{V}_{\mathrm{L}}$) and right ($\mathbf{V}_{\mathrm{R}}$) states and the solution ($\mathbf{V}$) are close to a constant state ($\overline{\mathbf{V}}$), the primitive form of the Eq. (10) can be replaced by a quasi-linear system of equation,

$$\frac{\partial \mathbf{V}}{\partial t} + \overline{\mathbf{A}} \cdot \nabla \mathbf{V} = \frac{\partial \mathbf{V}}{\partial t} + (\overline{\mathbf{A}}_x, \overline{\mathbf{A}}_y) \cdot \nabla \mathbf{V} = 0, \tag{13}$$

where $\overline{\mathbf{A}} \equiv \overline{\mathbf{A}}(\overline{\mathbf{V}}) = \overline{\mathbf{A}}(\mathbf{V}_{\mathrm{L}}, \mathbf{V}_{\mathrm{R}})$.

In 1D MHD, the full set of eight MHD equations can be reduced to seven of them as the gradient of the normal magnetic field should be zero, and such a constant normal field is not to be evaluated. For multidimensional MHD, however, the terms $\partial B_x/\partial x$ and $\partial B_y/\partial y$ in the full MHD equations do not vanish in general, and they play crucial roles that cannot be ignored.

In order to include the gradient terms for multidimensional MHD in a data reconstruction–evolution formulation, we present an approach which is built upon a dimensionally-unsplit second-order MUSCL-Hancock algorithm.

We treat the evolution of the normal field, B_{N}, separately from the other primitive variables, i.e., for a case with $B_{\mathrm{N}} = B_x$, we define

$$\overline{\mathbf{V}} = \begin{bmatrix} \widehat{\mathbf{V}} \\ B_x \end{bmatrix} \quad \text{and} \quad \overline{\mathbf{A}}_x = \begin{bmatrix} \widehat{\mathbf{A}}_x & \mathbf{A}_{B_x} \\ \mathbf{0} & 0 \end{bmatrix}. \tag{14}$$

Here $\widehat{\mathbf{V}}$ is a 7×1 vector excluding B_x, $\widehat{\mathbf{A}}_x$ is a 7×7 matrix omitting both the fifth row and column in the original matrix $\mathbf{A}_x$ (11), and $\mathbf{A}_{B_x}$ is a 7×1 vector,

$$\mathbf{A}_{B_x} = \left[0, -\frac{B_x}{\rho}, -\frac{B_y}{\rho}, -\frac{B_z}{\rho}, -v, -w, -k\mathbf{u} \cdot \mathbf{B}\right]^{\mathrm{T}}. \tag{15}$$

Similarly, for $B_{\mathrm{N}} = B_y$, $\widehat{\mathbf{A}}_y$ is constructed by omitting both the sixth row and column in the original matrix $\mathbf{A}_y$ (12), and $\mathbf{A}_{B_y}$ is

$$\mathbf{A}_{B_y} = \left[0, -\frac{B_x}{\rho}, -\frac{B_y}{\rho}, -\frac{B_z}{\rho}, -u, -w, -k\mathbf{u} \cdot \mathbf{B}\right]^{\mathrm{T}}. \tag{16}$$

A similar approach was adopted by Crockett et al. [9] but their equivalent terms for $\widehat{\mathbf{A}}_x$ and $\widehat{\mathbf{A}}_y$ omitted the factor k in the last entry, probably typographically. The terms in $\mathbf{A}_{B_x}$ and $\mathbf{A}_{B_y}$ will be referred to as "multidimensional MHD terms" in the following. Note that the hat ($\hat{\ }$) notation has been introduced for the reduced system (i.e., the one corresponding to the usual 1D MHD equations) and the bar ($\bar{\ }$) notation retained for the re-assembled full system.

The data reconstruction–evolution of the four multidimensional Riemann states $\mathbf{V}^{n+1/2}_{i,j,N,S,E,W}$ (see Fig. 1) at cell boundaries[1] is achieved to second-order accuracy by using a TVD MUSCL-Hancock approach. In extrapolating the cell center values to the cell interfaces we use a TVD slope limiter[2] applied to characteristic variables.

We mention an important strategy for employing TVD limiting at this stage. The limiting is applied to the cell-centered variables, such as density, velocity fields, and pressure, in both normal and transverse directions, while the limiting is applied only in the transverse direction for the cell-centered magnetic fields. Hence no limiting is applied to the normal field variables and we directly use the divergence-free field values from the previous time step at the cell faces. As a consequence, the C^0 continuity of the normal component of the magnetic field at cell faces is maintained. This strategy is based on numerical considerations to prevent undesirable jumps in the normal components of the fields at the cell boundaries. Indeed, Powell [31] noticed that if the normal fields have jumps at the cell boundaries, the resultant cell-centered MHD formulation using a Riemann solver becomes ill-defined. Powell et al. [32] eventually resolved this problem by introducing the 8-wave model with modified MHD equations. In the current scheme, using the divergence-free cell face (or cell face-centered) fields, the continuity consideration of the normal fields at the cell interfaces is met straightforwardly.

Given the quasi-linearized MHD equations,

$$\mathbf{V}^{n+1/2}_{i,j,E,W} = \mathbf{V}^n_{i,j} + \frac{1}{2}\left[\pm \mathbf{I} - \frac{\Delta t}{\Delta x}\mathbf{A}_x(\mathbf{V}^n_{i,j})\right]\Delta^n_i - \frac{\Delta t}{2\Delta y}\mathbf{A}_y(\mathbf{V}^n_{i,j})\Delta^n_j, \tag{17}$$

$$\mathbf{V}^{n+1/2}_{i,j,N,S} = \mathbf{V}^n_{i,j} - \frac{\Delta t}{2\Delta x}\mathbf{A}_x(\mathbf{V}^n_{i,j})\Delta^n_i + \frac{1}{2}\left[\pm \mathbf{I} - \frac{\Delta t}{\Delta y}\mathbf{A}_y(\mathbf{V}^n_{i,j})\right]\Delta^n_j, \tag{18}$$

where the plus and minus signs correspond to directions of N, E and S, W respectively, and $\mathbf{A}_x(\mathbf{V}^n_{i,j})$, $\mathbf{A}_x(\mathbf{V}^n_{i,j})$ represent matrices calculated at $\mathbf{V}^n_{i,j}$, we first consider a data reconstruction–evolution in the normal direction (e.g., the first two terms in the right hand side of (17)),

$$\begin{bmatrix} \widehat{\mathbf{V}} \\ B_x \end{bmatrix}^{n+1/2,\|}_{i,j,E,W} = \begin{bmatrix} \widehat{\mathbf{V}} \\ B_x \end{bmatrix}^{n}_{i,j} + \frac{1}{2}\left(\pm \begin{bmatrix} \widehat{\mathbf{I}} & \mathbf{0} \\ \mathbf{0} & 1 \end{bmatrix} - \frac{\Delta t}{\Delta x}\begin{bmatrix} \widehat{\mathbf{A}}_x & \mathbf{A}_{B_x} \\ \mathbf{0} & 0 \end{bmatrix}^n_{i,j}\right)\overline{\Delta}^n_i, \tag{19}$$

---

[1] As is usual, N, S, E, W are such that $(\mathbf{V}_{i-1,j,E}, \mathbf{V}_{i,j,W})$ are left–right pairs across the cell face located at $(i - 1/2)$, etc.

[2] For instance, one of the slope limiters such as Minmod, van Leer's, MC, or a combination of them on different wave structures [4] can be used.

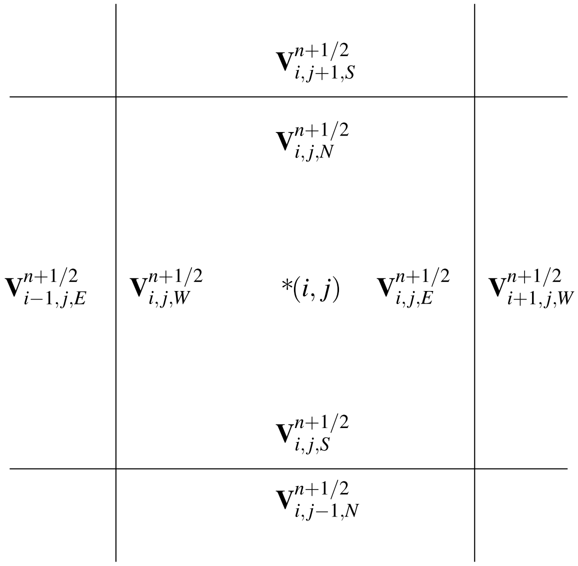

Fig. 1. The boundary extrapolated values on a 2D cell geometry. The values are subscripted by N, S, E, and W accordingly. These are used as the state values for solving a Riemann problem at each cell interface.

where $\overline{\Delta}^n_i = \left(\widehat{\Delta}^n_i, \Delta B^n_{x,i}\right)^{\mathrm{T}}$ and $\Delta B^n_{x,i} = b^n_{x,i+1/2,j} - b^n_{x,i-1/2,j}$ (the meaning of $\widehat{\Delta}^n_i$ becoming clear shortly). The notation B_τ and b_τ denote cell-centered and cell face-centered magnetic field components, respectively, with $\tau = x, y, z$. In the staggered mesh CT algorithm, $\Delta B^n_{x,i}$ is constructed such that the numerical divergence is zero using the cell face-centered magnetic fields. In other words, $\Delta B^n_{x,i}$ and $\Delta B^n_{y,j}$ are chosen such that

$$\frac{\Delta B^n_{x,i}}{\Delta x} + \frac{\Delta B^n_{y,j}}{\Delta y} = 0, \tag{20}$$

where we analogously define $\Delta B^n_{y,j} = b^n_{y,i,j+1/2} - b^n_{y,i,j-1/2}$. As noted previously no TVD limiting is applied to $\Delta B^n_{x,i}$ or $\Delta B^n_{y,j}$. Solving (19) is equivalent to considering two subsystems

$$\begin{cases} \widehat{\mathbf{V}}^{n+1/2,\|}_{i,j,E,W} = \widehat{\mathbf{V}}^n_{i,j} + \frac{1}{2}\left(\pm\widehat{\mathbf{I}} - \frac{\Delta t}{\Delta x}\widehat{\mathbf{A}}_x\right)^n_{i,j}\widehat{\Delta}^n_i - \frac{\Delta t}{2\Delta x}(\mathbf{A}_{B_x})^n_{i,j}\Delta B^n_{x,i}, \\ (B_x)^{n+1/2,\|}_{i,j,E,W} = B^n_{x,i,j} \pm \frac{1}{2}\Delta B^n_{x,i}, \end{cases} \tag{21}$$

where the second relation in (21) becomes

$$(B_x)^{n+1/2,\|}_{i,j,E,W} = B^n_{x,i,j} \pm \frac{1}{2}\Delta B^n_{x,i} = b^n_{x,i\pm1/2,j}, \tag{22}$$

if the cell-centered magnetic field is reconstructed as

$$B^n_{x,i,j} = \frac{1}{2}(b^n_{x,i+1/2,j} + b^n_{x,i-1/2,j}). \tag{23}$$

We apply the eigenstructure of the 1D based MHD equations and use characteristic information for the first two terms in the first equation in (21),

$$\widehat{\mathbf{V}}^{n+1/2,\|}_{i,j,W} = \widehat{\mathbf{V}}^n_{i,j} + \frac{1}{2}\sum_{k;\lambda^k_{i,j}<0}\left(-1 - \frac{\Delta t}{\Delta x}\lambda^k_{i,j}\right)\mathbf{r}^k_{x,i,j}\widehat{\Delta}\alpha^n_i - \frac{\Delta t}{2\Delta x}(\mathbf{A}_{B_x})^n_{i,j}\Delta B^n_{x,i}, \tag{24}$$

$$\widehat{\mathbf{V}}^{n+1/2,\|}_{i,j,E} = \widehat{\mathbf{V}}^n_{i,j} + \frac{1}{2}\sum_{k;\lambda^k_{i,j}>0}\left(1 - \frac{\Delta t}{\Delta x}\lambda^k_{i,j}\right)\mathbf{r}^k_{x,i,j}\widehat{\Delta}\alpha^n_i - \frac{\Delta t}{2\Delta x}(\mathbf{A}_{B_x})^n_{i,j}\Delta B^n_{x,i} \tag{25}$$

with characteristic limiting in the normal direction,

$$\widehat{\Delta}\alpha^n_i = \mathtt{TVD\_Limiter}\left[\mathbf{l}^k_{x,i,j}\cdot\widehat{\Delta}^n_{i,+}, \mathbf{l}^k_{x,i,j}\cdot\widehat{\Delta}^n_{i,-}\right]. \tag{26}$$

Here $\lambda^k_{x,i,j}, \mathbf{r}^k_{x,i,j}, \mathbf{l}^k_{x,i,j}$ represent, respectively, the eigenvalue, right, and left eigenvectors of $\widehat{\mathbf{A}}_x$, calculated at the corresponding cell center (i,j) in the x-direction at time step n, and $\widehat{\Delta}^n_{i,+} = \widehat{\mathbf{V}}^n_{i+1,j} - \widehat{\mathbf{V}}^n_{i,j}$, $\widehat{\Delta}^n_{i,-} = \widehat{\mathbf{V}}^n_{i,j} - \widehat{\mathbf{V}}^n_{i-1,j}$ (similarly for $\widehat{\Delta}^n_{j,\pm}$).

One useful correction to preserve second-order accuracy in this normal update using the characteristic tracing method has been observed by Stone et al. [18] when employing approximate Riemann solvers that are based on averaging left and right intermediate states (e.g., the HLL-type of Riemann solvers, but not the Roe or exact Riemann solvers). A correction becomes useful in situations where waves propagate away from the interface, e.g., at $(i+1/2,j)$. In such case, both $\widehat{\mathbf{V}}^{n+1/2,\|}_{i,j,E}$ and $\widehat{\mathbf{V}}^{n+1/2,\|}_{i+1,j,W}$ would not have any of the predicted half time step solutions, therefore the resultant solution at $n+1$ time step will be first-order. Taking this into consideration, when the HLL-type of Riemann solvers are used in simulation, we modify Eqs. (24) and (25) as

$$\widehat{\mathbf{V}}^{n+1/2,\|}_{i,j,W} = \widehat{\mathbf{V}}^{n}_{i,j} + \frac{1}{2}\sum_{k=1}^{7}\left(-1-\frac{\Delta t}{\Delta x}\lambda^k_{i,j}\right)\mathbf{r}^k_{x,i,j}\widehat{\Delta}\alpha^n_i - \frac{\Delta t}{2\Delta x}(\mathbf{A}_{B_x})^n_{i,j}\Delta B^n_{x,i}, \tag{27}$$

$$\widehat{\mathbf{V}}^{n+1/2,\|}_{i,j,E} = \widehat{\mathbf{V}}^{n}_{i,j} + \frac{1}{2}\sum_{k=1}^{7}\left(1-\frac{\Delta t}{\Delta x}\lambda^k_{i,j}\right)\mathbf{r}^k_{x,i,j}\widehat{\Delta}\alpha^n_i - \frac{\Delta t}{2\Delta x}(\mathbf{A}_{B_x})^n_{i,j}\Delta B^n_{x,i}. \tag{28}$$

The next step includes the transverse flux contribution to the calculated normal state variables. This transverse step, using the eigenstructure of the MHD equations, completes the update from the y-flux contributions, e.g., the third and second terms in (17) and (18), respectively. For instance, in (17) the transverse step can be updated as

$$\mathbf{V}^{n+1/2}_{i,j,E,W} = \mathbf{V}^{n+1/2,\|}_{i,j,E,W} - \frac{\Delta t}{2\Delta y}\mathbf{A}_y(\mathbf{V}^n_{i,j})\Delta^n_j. \tag{29}$$

Again, this can be written as

$$\begin{bmatrix}\widehat{\mathbf{V}}\\ B_y\end{bmatrix}^{n+1/2}_{i,j,E,W} = \begin{bmatrix}\widehat{\mathbf{V}}\\ B_y\end{bmatrix}^{n+1/2,\|}_{i,j,E,W} - \frac{\Delta t}{2\Delta y}\begin{bmatrix}\widehat{\mathbf{A}}_y & \mathbf{A}_{B_y}\\ \mathbf{0} & 0\end{bmatrix}^n_{i,j}\overline{\Delta}^n_j, \tag{30}$$

which reduces to solve just one subsystem,

$$\widehat{\mathbf{V}}^{n+1/2}_{i,j,E,W} = \widehat{\mathbf{V}}^{n+1/2,\|}_{i,j,E,W} - \frac{\Delta t}{2\Delta y}(\widehat{\mathbf{A}}_y)^n_{i,j}\widehat{\Delta}^n_j - \frac{\Delta t}{2\Delta y}(\mathbf{A}_{B_y})^n_{i,j}\Delta B^n_{y,j}. \tag{31}$$

Using the eigensystem at the cell center (i,j) in the y-direction, we get,

$$\widehat{\mathbf{V}}^{n+1/2}_{i,j,E,W} = \widehat{\mathbf{V}}^{n+1/2,\|}_{i,j,E,W} - \frac{\Delta t}{2\Delta y}\sum_{k=1}^{7}\lambda^k_{y,i,j}\mathbf{r}^k_{y,i,j}\widetilde{\Delta}\alpha^n_j - \frac{\Delta t}{2\Delta y}(\mathbf{A}_{B_y})^n_{i,j}\Delta B^n_{y,j}, \tag{32}$$

where an upwinding slope $\widetilde{\Delta}\alpha^n_j = \mathtt{Upwinding}\left[\mathbf{l}^k_{y,i,j}\cdot\widehat{\Delta}^n_{j,+}, \mathbf{l}^k_{y,i,j}\cdot\widehat{\Delta}^n_{j,-}\right]$ is given by

$$\widetilde{\Delta}\alpha^n_j = \begin{cases}\mathbf{l}^k_{y,i,j}\cdot\widehat{\Delta}^n_{j,+} & \text{if } \lambda^k_{y,i,j} < 0,\\ \mathbf{l}^k_{y,i,j}\cdot\widehat{\Delta}^n_{j,-} & \text{if } \lambda^k_{y,i,j} > 0.\end{cases} \tag{33}$$

Note that in (32) we sum over contributions from all waves for the transverse fluxes. This can be viewed in general, via simple consideration of jumps across waves. Given eigenvalues λ^k, $k = 1,\ldots,7$, ordered as

$$\lambda^1 \leqslant \cdots \leqslant 0 \leqslant \lambda^{k_0} \leqslant \cdots \leqslant \lambda^k, \quad k_0 \leqslant k, \tag{34}$$

the property of conservation across discontinuities of the Roe matrices $\widehat{\mathbf{A}}_x$ and $\widehat{\mathbf{A}}_y$ in (11) and (12) gives (dropping indices and using left and right terminologies for convenience),

$$\widehat{\mathbf{A}}\widehat{\Delta} = \widehat{\mathbf{A}}(\widehat{\mathbf{V}}_{\mathrm{r}} - \widehat{\mathbf{V}}_{\mathrm{l}}) = \mathtt{Flux}(\mathbf{V}_{\mathrm{r}}) - \mathtt{Flux}(\mathbf{V}_{\mathrm{l}}). \tag{35}$$

As the left and right states are related via a simple jump relationship,

$$\widehat{\mathbf{A}}\widehat{\mathbf{V}}_{\mathrm{l}} + \sum_{k=1}^{k_0-1}\lambda^k\mathbf{r}^{\mathbf{k}}\widetilde{\Delta}\alpha = \widehat{\mathbf{A}}\widehat{\mathbf{V}}_{\mathrm{r}} - \sum_{k=k_0}^{7}\lambda^k\mathbf{r}^{\mathbf{k}}\widetilde{\Delta}\alpha, \tag{36}$$

we see that the sum over all wave contributions gives an effective upwinding of transverse flux gradients. Note, in (24) and (25), however, we restrict the wave contributions on the physical consideration of the left- and right-going waves separately using a characteristic tracing method (see [8]).

Thus far we have obtained four Riemann states $\mathbf{V}^{n+1/2}_{i,j,N,S,E,W}$ that are second-order accurate at $n+1/2$ time step for all variables *except* the normal fields at each cell interface (boundary). We require two conditions in obtaining such normal fields: a continuity restriction across cell interfaces and the divergence-free constraint. Maintaining the continuity requirement of the normal fields at the interfaces has been previously recognized as an important issue in the MHD Riemann problem [4,9,16,31]. This requirement is essential for physical consistency. Computationally, allowing jumps in the normal fields at the cell interfaces can lead to more diffusive solutions to Riemann problems stemming from the upwinding procedure in the Riemann solvers. For the transverse components of the magnetic field, however, discontinuities are allowed and mediate the proper upwinding for them. As a last step, therefore, we evolve the normal field components at each cell boundary by a half time step, following the CT approach using the high-order Godunov fluxes that are solutions to a Riemann problem (RP for short) of the above Riemann states $\mathbf{V}^{n+1/2}_{i,j,N,S,E,W}$. Practically, we first solve

$$\widetilde{\mathbf{F}}^{*,n+1/2}_{i-1/2,j} = \mathrm{RP}\left(\mathbf{V}^{n+1/2}_{i-1,j,E}, \mathbf{V}^{n+1/2}_{i,j,W}\right), \quad \widetilde{\mathbf{F}}^{*,n+1/2}_{i+1/2,j} = \mathrm{RP}\left(\mathbf{V}^{n+1/2}_{i,j,E}, \mathbf{V}^{n+1/2}_{i+1,j,W}\right) \tag{37}$$

and

$$\widetilde{\mathbf{G}}^{*,n+1/2}_{i,j-1/2} = \mathrm{RP}\left(\mathbf{V}^{n+1/2}_{i,j-1,N}, \mathbf{V}^{n+1/2}_{i,j,S}\right), \quad \widetilde{\mathbf{G}}^{*,n+1/2}_{i,j+1/2} = \mathrm{RP}\left(\mathbf{V}^{n+1/2}_{i,j,N}, \mathbf{V}^{n+1/2}_{i,j+1,S}\right). \tag{38}$$

Based on these fluxes at the half time step we update the normal fields by a half time step as

$$b^{n+1/2}_{x,i+1/2,j} = b^{n}_{x,i+1/2,j} - \frac{\Delta t}{2\Delta y}\left\{\widetilde{E}^{n+1/2}_{z,i+1/2,j+1/2} - \widetilde{E}^{n+1/2}_{z,i+1/2,j-1/2}\right\}, \tag{39}$$

$$b^{n+1/2}_{y,i,j+1/2} = b^{n}_{y,i,j+1/2} - \frac{\Delta t}{2\Delta x}\left\{-\widetilde{E}^{n+1/2}_{z,i+1/2,j+1/2} + \widetilde{E}^{n+1/2}_{z,i-1/2,j+1/2}\right\}, \tag{40}$$

where the duality relationship between the electric fields (e.g., $\widetilde{E}^{n+1/2}_z$) and the high-order Godunov fluxes (e.g., $\widetilde{\mathbf{F}}^*, \widetilde{\mathbf{G}}^*$) are assumed and will be described in more detail in the next section (e.g., see (47)). These normal fields satisfy the divergence-free constraint as well as the continuity restriction across cell interfaces as they are direct solutions to numerical induction equations via the CT approach. Given these fields we update the previously obtained four Riemann states as

$$\mathbf{V}^{n+1/2}_{i,j,N} \cdot \mathbf{e}_{B_y} = b^{n+1/2}_{y,i,j+1/2}, \quad \mathbf{V}^{n+1/2}_{i,j,S} \cdot \mathbf{e}_{B_y} = b^{n+1/2}_{y,i,j-1/2}, \tag{41}$$

$$\mathbf{V}^{n+1/2}_{i,j,E} \cdot \mathbf{e}_{B_x} = b^{n+1/2}_{x,i+1/2,j}, \quad \mathbf{V}^{n+1/2}_{i,j,W} \cdot \mathbf{e}_{B_x} = b^{n+1/2}_{x,i-1/2,j}, \tag{42}$$

where **e** are unit vectors for the magnetic field components, respectively.

The algorithm for our Riemann state data reconstruction–evolution is based on the method of multidimensional characteristic analysis that can be achieved in a single step, without solving a separate Riemann problem for transverse flux gradients. The importance of the present scheme lies in the fact that the multidimensional MHD terms are included and balanced simultaneously in the quasi-linearized form of the MHD equations in a consistent way using the characteristic analysis for both normal and transverse flux gradients. It is also evident that the extension to 3D is straightforward: for instance, we only need to add additional upwinding transverse flux gradient from z-direction (e.g., $\sum_{k=1}^{7}\lambda^k_z \mathbf{r}^k_z \widetilde{\Delta}\alpha^n$) along with the multidimensional MHD term in z-direction (e.g., $\mathbf{A}^n_{B_z}\Delta B^n_z$) in Eq. (32).

Note that a typical unsplit CTU scheme in multidimensions, originally by Colella [8], would need to solve four Riemann problems in 2D and 12 in 3D [37] per zone per time step. In 2D MHD one recent approach to obtain second-order accurate approximations of the transverse flux derivatives can be found in [9]. There the transverse predictor updating step used the normal predictor step values to solve another intermediate Riemann problem. The resulting interface fluxes were then used to take numerical derivatives, completing their data reconstruction–evolution of the Riemann states in the predictor step. More recently, Gardiner and Stone generalized a new 3D CTU scheme for MHD that only involves six Riemann problems [17].

The current data reconstruction–evolution method, which accommodates the MHD eigenstructure multidimensionally in a single step, is simpler and computationally less expensive in evaluating the transverse flux gradients. The characteristic method is mathematically consistent with the quasi-linearized system of MHD equations, and causes no loss of stability for appropriately chosen Courant numbers. Along with the current data reconstruction–evolution algorithm, the overall integration scheme requires the solution of four Riemann problems in 2D and six in 3D. Details of the 3D implementation will appear in a future paper.

Turning back to the practical significance of our data reconstruction–evolution algorithm, the most desirable aspect can be seen in that the multidimensional MHD terms $\mathbf{A}_{B_x}$ and $\mathbf{A}_{B_y}$ are included such that they are proportional to $\Delta B_{x,i}/\Delta x$ and $\Delta B_{y,j}/\Delta y$. These derivatives are computed using the cell face magnetic fields that are divergence-free from the CT-type formulation in the USM scheme. This fact implies that the quantities u, v, w, B_z, p are all evolved proportional to the sum $\frac{\Delta B_{x,i}}{\Delta x} + \frac{\Delta B_{y,j}}{\Delta y}$, which is vanishingly small numerically (see (20)). As a result, this dependence has an important meaning: if perturbations to the divergence $\frac{\Delta B_{x,i}}{\Delta x} + \frac{\Delta B_{y,j}}{\Delta y}$ were to be introduced, such perturbation would affect the behavior of all of u, v, w, B_z, p. For example, as noted by Gardiner and Stone [16], maintaining planar dynamics in 2D MHD problems by not allowing erroneous growth of the B_z component is directly dependent on how the terms $\Delta B_{x,i}/\Delta x$ and $\Delta B_{y,j}/\Delta y$ are handled in the data reconstruction–evolution step. In the current multidimensional data reconstruction–evolution algorithm such growth in B_z is avoided, and its success is illustrated in the in-plane field loop advection test in Section 5.

Now that the second-order accurate Riemann states, $\mathbf{V}^{n+1/2}_{i,j,N,S,E,W}$, are available, the second-order Godunov fluxes can be evaluated by solving Riemann problems at cell interfaces. That is,

$$\mathbf{F}^{*,n+1/2}_{i-1/2,j} = \mathrm{RP}\left(\mathbf{V}^{n+1/2}_{i-1,j,E}, \mathbf{V}^{n+1/2}_{i,j,W}\right), \quad \mathbf{F}^{*,n+1/2}_{i+1/2,j} = \mathrm{RP}\left(\mathbf{V}^{n+1/2}_{i,j,E}, \mathbf{V}^{n+1/2}_{i+1,j,W}\right), \tag{43}$$

$$\mathbf{G}^{*,n+1/2}_{i,j-1/2} = \mathrm{RP}\left(\mathbf{V}^{n+1/2}_{i,j-1,N}, \mathbf{V}^{n+1/2}_{i,j,S}\right), \quad \mathbf{G}^{*,n+1/2}_{i,j+1/2} = \mathrm{RP}\left(\mathbf{V}^{n+1/2}_{i,j,N}, \mathbf{V}^{n+1/2}_{i,j+1,S}\right). \tag{44}$$

Note that the superscript $*$ is used to represent the second-order Godunov fluxes that are the solutions of the Riemann problems.

2.2. The USM cell-centered solution update

The algorithm updates the cell-centered conservative variables to the next time step $n+1$ using an unsplit integrator,

$$\mathbf{U}_{i,j}^{n+1} = \mathbf{U}_{i,j}^{n} - \frac{\Delta t}{\Delta x}\left\{\mathbf{F}_{i+1/2,j}^{*,n+1/2} - \mathbf{F}_{i-1/2,j}^{*,n+1/2}\right\} - \frac{\Delta t}{\Delta y}\left\{\mathbf{G}_{i,j+1/2}^{*,n+1/2} - \mathbf{G}_{i,j-1/2}^{*,n+1/2}\right\}. \tag{45}$$

In general, after this update, non-zero divergence magnetic fields are still present at cell centers, and they need to be corrected. In the next section we describe a new modified electric field construction (MEC) scheme which is used in the CT algorithm for the discrete induction equations to keep the cell face magnetic fields divergence-free numerically. The cell-centered magnetic fields are then corrected using these cell face fields.

The choice of a time step Δt for our unsplit scheme is limited by a CFL condition (in 2D),

$$\Delta t\left(\frac{\left|\lambda_{x,i,j}^{\max}\right|}{\Delta x}, \frac{\left|\lambda_{y,i,j}^{\max}\right|}{\Delta y}\right) \leqslant c. \tag{46}$$

We use a CFL number, $c = 0.8$ for all calculations, except where otherwise noted.

3. Construction of electric fields

A new modified electric field construction (MEC) scheme that retains full directional information is introduced and studied in this section. The MEC scheme is obtained by using the second-order accurate Godunov fluxes that are available from the data reconstruction–evolution scheme in Section 2. Taylor expansions are applied to the flux components of the magnetic fields (or electric fields by the duality relationship [2]) at the face centers to obtain extrapolations at each cell corner where the electric field is collocated. The electric fields at cell corners are then used in the discrete induction equations to evolve divergence-less magnetic fields at cell faces.

3.1. Simple electric field averaging scheme

The CT based scheme requires the evaluation of the electric field **E**. Balsara and Spicer [2] proposed to evaluate the electric field on a staggered mesh using the duality relationship between the electric fields and high-order Godunov fluxes and taking a simple arithmetic average over the cell face-centered fluxes

$$E_{z,i+1/2,j+1/2}^{n+1/2} = \frac{1}{4}\left\{-F_{6,i+1/2,j}^{*,n+1/2} - F_{6,i+1/2,j+1}^{*,n+1/2} + G_{5,i,j+1/2}^{*,n+1/2} + G_{5,i+1,j+1/2}^{*,n+1/2}\right\} = \frac{1}{4}\left\{E_{z,i+1/2,j}^{*,n+1/2} + E_{z,i+1/2,j+1}^{*,n+1/2} + E_{z,i,j+1/2}^{*,n+1/2} + E_{z,i+1,j+1/2}^{*,n+1/2}\right\}. \tag{47}$$

The subscripts 6 and 5 denote the sixth and fifth components in the corresponding flux vectors in Eq. (9), and the superscript $*$ denotes the fluxes (or flux components) directly from the high-order Godunov schemes. See Fig. 2 for the staggered mesh arrangement in 2D.

The electric field E_z in Eq. (47) can be used to update the induction equations in an appropriate discretization in different MHD solvers. To discretize the induction equations in a more general sense, we consider integrating the differential form (1) over a single 3D control volume $\left[i-\frac{1}{2}, i+\frac{1}{2}\right] \times \left[j-\frac{1}{2}, j+\frac{1}{2}\right] \times \left[k-\frac{1}{2}, k+\frac{1}{2}\right]$ in a Cartesian staggered grid. Taking a surface integral of the induction equations and applying Stokes' theorem yields

$$b_\eta^n = \frac{1}{A(\mathcal{F}_\ell)} {}_{\mathcal{F}_\ell} B_\eta \,\mathrm{d}A, \quad E_\tau^{n+1/2} = \frac{1}{L(\partial\mathcal{F}_\ell)} \int_{\partial\mathcal{F}_\ell} E_\tau \,\mathrm{d}l, \tag{48}$$

where A and L are the respective area and length and $\eta, \tau = x, y, z$, with the six bounding faces $\mathcal{F}_\ell$, $\ell = 1, \ldots, 6$. Note that in the CT formulation the magnetic field components b_η^n are the area-averaged values at cell faces, whereas the rest of the conservative variables such as the density, momentum, and energy are volume-averaged quantities. Using (48) it is straightforward to rewrite the induction equations at each control volume's face in component-wise form as

$$\Delta y \Delta z \frac{\partial}{\partial t} b_{x,i\pm\frac{1}{2},j,k}^n = -\left\{\Delta z\left(E_{z,i\pm\frac{1}{2},j+\frac{1}{2},k}^{n+1/2} - E_{z,i\pm\frac{1}{2},j-\frac{1}{2},k}^{n+1/2}\right) + \Delta y\left(E_{y,i\pm\frac{1}{2},j,k-\frac{1}{2}}^{n+1/2} - E_{y,i\pm\frac{1}{2},j,k+\frac{1}{2}}^{n+1/2}\right)\right\}, \tag{49}$$

$$\Delta x \Delta z \frac{\partial}{\partial t} b_{y,i,j\pm\frac{1}{2},k}^n = -\left\{\Delta z\left(E_{z,i-\frac{1}{2},j\pm\frac{1}{2},k}^{n+1/2} - E_{z,i+\frac{1}{2},j\pm\frac{1}{2},k}^{n+1/2}\right) + \Delta x\left(E_{x,i,j\pm\frac{1}{2},k+\frac{1}{2}}^{n+1/2} - E_{x,i,j\pm\frac{1}{2},k-\frac{1}{2}}^{n+1/2}\right)\right\}. \tag{50}$$

Further, by discretizing the temporal derivative terms and dividing out Δx, Δy, and Δz, we obtain discrete form of the induction equations on the staggered grid. For instance, in 2D, we get the original Yee's method [42] by applying the forward temporal discretization

$$b_{x,i+1/2,j}^{n+1} = b_{x,i+1/2,j}^{n} - \frac{\Delta t}{\Delta y}\left\{E_{z,i+1/2,j+1/2}^{n+1/2} - E_{z,i+1/2,j-1/2}^{n+1/2}\right\}, \tag{51}$$

$$b_{y,i,j+1/2}^{n+1} = b_{y,i,j+1/2}^{n} - \frac{\Delta t}{\Delta x}\left\{-E_{z,i+1/2,j+1/2}^{n+1/2} + E_{z,i-1/2,j+1/2}^{n+1/2}\right\}. \tag{52}$$

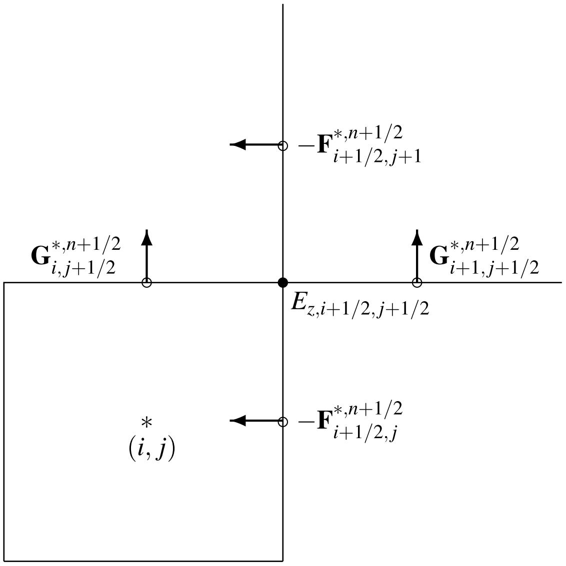

Fig. 2. A schematic 2D geometry of the staggered mesh in the flux-CT finite volume scheme. In the staggered mesh, the upwinded numerical fluxes $\mathbf{F}^*$ and $\mathbf{G}^*$ are collocated at the centers of cell interfaces and the electric fields $\mathbf{E}$ (only E_z is shown here for 2D) are collocated at the cell corners.

Most CT schemes [2–4,16,17] essentially make the above discretization. On a staggered grid, the numerical divergence of $\mathbf{B}$ is defined by

$$(\nabla\cdot\mathbf{B})^{n+1}_{i,j} = \frac{b^{n+1}_{x,i+1/2,j} - b^{n+1}_{x,i-1/2,j}}{\Delta x} + \frac{b^{n+1}_{y,i,j+1/2} - b^{n+1}_{y,i,j-1/2}}{\Delta y} \tag{53}$$

and it remains zero to machine round-off, provided that $(\nabla\cdot\mathbf{B})^{n}_{i,j} = 0$.

3.2. MEC algorithm using directional derivatives in the electric field construction

We now describe a new electric field construction scheme that uses first- and second-order directional derivatives evaluated at cell faces to extrapolate the electric fields to cell corners. The cell face electric fields are available from corresponding components of the high-order Godunov fluxes that are solutions to the Riemann problem. The superscript "$*$" is used, consistent with the previous section.

Using a Taylor series expansion of the cell-cornered electric field $E^{n+1/2}_{z,i+1/2,j+1/2}$ in all directions, we can write

$$\begin{cases} E^{n+1/2}_{z,i+1/2,j+1/2} = E^{*,n+1/2}_{z,i+1/2,j} + \frac{\Delta y}{2}\frac{\partial E^{*,n+1/2}_{z,i+1/2,j}}{\partial y} + \frac{\Delta y^2}{8}\frac{\partial^2 E^{*,n+1/2}_{z,i+1/2,j}}{\partial y^2} + \mathcal{O}(\Delta y^3), \\ E^{n+1/2}_{z,i+1/2,j+1/2} = E^{*,n+1/2}_{z,i+1/2,j+1} - \frac{\Delta y}{2}\frac{\partial E^{*,n+1/2}_{z,i+1/2,j+1}}{\partial y} + \frac{\Delta y^2}{8}\frac{\partial^2 E^{*,n+1/2}_{z,i+1/2,j+1}}{\partial y^2} + \mathcal{O}(\Delta y^3), \\ E^{n+1/2}_{z,i+1/2,j+1/2} = E^{*,n+1/2}_{z,i,j+1/2} + \frac{\Delta x}{2}\frac{\partial E^{*,n+1/2}_{z,i,j+1/2}}{\partial x} + \frac{\Delta x^2}{8}\frac{\partial^2 E^{*,n+1/2}_{z,i,j+1/2}}{\partial x^2} + \mathcal{O}(\Delta x^3), \\ E^{n+1/2}_{z,i+1/2,j+1/2} = E^{*,n+1/2}_{z,i+1,j+1/2} - \frac{\Delta x}{2}\frac{\partial E^{*,n+1/2}_{z,i+1,j+1/2}}{\partial x} + \frac{\Delta x^2}{8}\frac{\partial^2 E^{*,n+1/2}_{z,i+1,j+1/2}}{\partial x^2} + \mathcal{O}(\Delta x^3). \end{cases} \tag{54}$$

The new *modified electric field construction* (MEC) algorithm takes an arithmetic average of these four Taylor expansions, yielding

$$\begin{aligned} E^{n+1/2}_{z,i+1/2,j+1/2} = \frac{1}{4}\Big\{ & E^{*,n+1/2}_{z,i+1/2,j} + \frac{\Delta y}{2}\left(\partial E^{*,n+1/2}_{z,i+1/2,j}/\partial y\right) + \frac{\Delta y^2}{8}\left(\partial^2 E^{*,n+1/2}_{z,i+1/2,j}/\partial y^2\right) + E^{*,n+1/2}_{z,i+1/2,j+1} - \frac{\Delta y}{2}\left(\partial E^{*,n+1/2}_{z,i+1/2,j+1}/\partial y\right) \\ & + \frac{\Delta y^2}{8}\left(\partial^2 E^{*,n+1/2}_{z,i+1/2,j+1}/\partial y^2\right) + E^{*,n+1/2}_{z,i,j+1/2} + \frac{\Delta x}{2}\left(\partial E^{*,n+1/2}_{z,i,j+1/2}/\partial x\right) + \frac{\Delta x^2}{8}\left(\partial^2 E^{*,n+1/2}_{z,i,j+1/2}/\partial x^2\right) + E^{*,n+1/2}_{z,i+1,j+1/2} \\ & - \frac{\Delta x}{2}\left(\partial E^{*,n+1/2}_{z,i+1,j+1/2}/\partial x\right) + \frac{\Delta x^2}{8}\left(\partial^2 E^{*,n+1/2}_{z,i+1,j+1/2}/\partial x^2\right)\Big\}. \end{aligned} \tag{55}$$

The inclusion of the directional derivative terms at this stage has several important aspects. In the CT-type of schemes the magnetic fields (surface variables) are evolved by solving the discretized induction equations (e.g., Eqs. (51) and (52)), whereas other conservative (volumetric) variables such as the density, momentum, and energy are updated by solving the underlying high-order Godunov scheme. These two sets of variables are updated differently, which does not mean that the surface and volumetric variables form two decoupled systems; rather, they are strongly coupled via the momentum, energy, and induction equations. Therefore, in order to obtain an overall accurate solution for both surface and volumetric variables they must be evaluated with consistent high-order accuracy. The derivative terms in Eq. (55) provide the needed accuracy as compared to the simple averaging scheme of Eq. (47).

The MEC algorithm in (55) is ideally third-order in space for smooth profiles of the electric fields. Note that the simple averaging scheme (47) only incorporates the smooth part of the electric fields by taking simple arithmetic averages of the electric field components at cell faces. The situation is improved in the MEC algorithm in such a way that the first derivative terms reflect correct spatial changes from the cell centers to the cell corners. Furthermore, the second derivative terms add proper amounts of dissipation to the extrapolated cell-cornered electric fields, avoiding spurious oscillations near discontinuities in solutions.

The MEC does not lead to a 1D form for grid-aligned plane–parallel flows. This can be important, shown in [16], as a lack of this property can lead to a lowering of numerical dissipation and hence introduce possible numerical instability. However, the amount of dissipation in our MEC algorithm, integrated in the whole USM scheme, is controlled adequately as shown in our tests such as the field loop advection. For plane–parallel flows, we explicitly tested such as the grid-aligned Brio–Wu shock tube or Alfvén wave propagation problems on 2D domains, and we have not found any instability issue in the results.

In discretizing the derivative terms in the MEC algorithm, two different approaches can be easily considered: central or upwinded differencing. For our purpose, we choose to use a central scheme for two reasons. First, an upwinded differencing requires a wider stencil (one more stencil point for each spatial direction) than a central differencing. The wider stencil means that more guard (or ghost) cells must be used for an upwinded differencing scheme, which is particularly a problem for parallel AMR grid structures where guard cells are used for boundary conditions and updated via inter-processor communications. Further, in multidimensions, extra guard cells require either more storage or more guard cell copy operations. For high levels of refinement this extra overhead can be a crucial issue. Second, an upwinding strategy becomes useful when that is used to obtain the direction of the propagation information in a flow field along the characteristics. The electric fields in ideal MHD, $\mathbf{E} = -\mathbf{u} \times \mathbf{B}$, nevertheless, do not propagate along the direction parallel to the velocity field, nor to the magnetic field. Gardiner and Stone [16] proposed an upwinded differencing according to the contact mode at each interface, which led to a stable, non-oscillatory integration algorithm. However, having implemented both alternatives we do not find any improvement in the solution using upwinded over central differencing. Thus for physical considerations as well for computational parallel efficiency, we choose a central differencing for discretizing the derivative terms in the MEC algorithm.

3.3. Central differencing for the MEC

A second-order central differencing is considered for both first and second derivative terms in the MEC algorithm. At x-interfaces (e.g., at $i \pm \frac{1}{2}$), we can discretize $\partial E^{*,n+1/2}_{z,i\pm1/2,j}/\partial y$ and $\partial^2 E^{*,n+1/2}_{z,i\pm1/2,j}/\partial y^2$ as

$$\frac{\partial E^{*,n+1/2}_{z,i\pm1/2,j}}{\partial y} = \frac{E^{*,n+1/2}_{z,i\pm1/2,j+1} - E^{*,n+1/2}_{z,i\pm1/2,j-1}}{2\Delta y} \tag{56}$$

and

$$\frac{\partial^2 E^{*,n+1/2}_{z,i\pm1/2,j}}{\partial y^2} = \frac{E^{*,n+1/2}_{z,i\pm1/2,j+1} - 2E^{*,n+1/2}_{z,i\pm1/2,j} + E^{*,n+1/2}_{z,i\pm1/2,j-1}}{\Delta y^2}. \tag{57}$$

Similarly, discretizations at y-interfaces (e.g., at $j \pm \frac{1}{2}$) are

$$\frac{\partial E^{*,n+1/2}_{z,i,j\pm1/2}}{\partial x} = \frac{E^{*,n+1/2}_{z,i+1,j\pm1/2} - E^{*,n+1/2}_{z,i-1,j\pm1/2}}{2\Delta x} \tag{58}$$

and

$$\frac{\partial^2 E^{*,n+1/2}_{z,i,j\pm1/2}}{\partial x^2} = \frac{E^{*,n+1/2}_{z,i+1,j\pm1/2} - 2E^{*,n+1/2}_{z,i,j\pm1/2} + E^{*,n+1/2}_{z,i-1,j\pm1/2}}{\Delta x^2}. \tag{59}$$

These derivatives are used in (55) and the subsequent electric fields are applied to the induction equations (51) and (52) for temporal evolutions of the divergence-free magnetic fields at cell interfaces (face centers).

4. Summary

We summarize the whole USM–MEC algorithm as follows:

(i) Calculate the second-order accurate MHD interfaces using the data reconstruction–evolution algorithm described in Section 2.1. The multidimensional MHD terms are included to balance terms that are proportional to $\nabla \cdot \mathbf{B} = 0$. The resulting MHD interface states are used to compute the first set of high-order Godunov fluxes by solving a Riemann problem (Eqs. (37) and (38) in Section 2.1).

(ii) The normal fields are evolved by a half time step at cell interfaces using the Godunov fluxes in step (i) (Eqs. (39) and (40) in Section 2.1).
(iii) Update the MHD interface states in step (i) with the calculated normal fields in step (ii) (Eqs. (41) and (42) in Section 2.1).
(iv) Solve the second set of Riemann problems at cell interfaces (Eqs. (43) and (44) in Section 2.1) and update the cell-centered conservative variables to the next time step (Eq. (45) in Section 2.2).
(v) Calculate the electric fields at cell corners by using the MEC algorithm described in Section 3.2. Using these electric fields the magnetic fields at cell faces are updated to the next time step (Eqs. (51) and (52) in Section 3.1). The cell-centered magnetic fields are updated using these divergence-free magnetic fields at cell face centers (e.g., Eq. (23) in Section 2.1).

5. Numerical results

Numerical studies of the USM–MEC scheme have been made with a suite of MHD test problems. These studies show that the scheme is very robust and second-order accurate, and maintains the solenoidal constraint of magnetic fields up to machine round-off error. The CFL number of 0.8 is used in all simulations. For the choice of the Riemann solvers we used the Roe-type linearized solver [33,39] and the HLLD solver [28].

In all of the multidimensional problems presented here, we demonstrate the excellent performance of the USM–MEC scheme, especially with: (a) our new multidimensional characteristic method in the data reconstruction–evolution step that truly combines multidimensional MHD terms in a single step (thus, obeying a perfect balance law of $\nabla \cdot \mathbf{B} = 0$); (b) an improved solution accuracy using the MEC scheme. Their roles are pointed out and found to be of importance.

5.1. Field loop problem

The first test is the field loop problem which is known to be one of stringent test cases in multidimensional MHD. In this test problem we consider an advection of a weakly magnetized field loop traversing the computational domain diagonally. Details of the problem has been described in [16] and we briefly discuss our setup here. We follow the parameters of Gardiner and Stone [16,38]. The computational domain is $[-1,1] \times [-0.5,0.5]$, with a grid resolution 256×148, and doubly-periodic boundary conditions. With this rectangular grid cell, the flow is not symmetric in x- and y-directions because the field loop does not advect across each *grid cell* diagonally and hence the resulting fluxes are different in x- and y-directions. The density and pressure are unity everywhere and $\gamma = 5/3$. The velocity fields are defined as

$$\mathbf{U} = u_0(\cos\theta, \sin\theta, 1) \tag{60}$$

with the advection angle θ, given by $\theta = \tan^{-1}(0.5) \approx 26.57^\circ$. For the choice of the initial advection velocity we set $u_0 = \sqrt{5}$. The size of domain and other parameters were chosen such that the weakly magnetized field loop makes one complete cycle by $t = 1$. It is important to initialize the magnetic fields to satisfy $\nabla \cdot \mathbf{B} = 0$ numerically in order to avoid any initial non-zero error in $\nabla \cdot \mathbf{B}$. As suggested in [16], the magnetic field components are initialized by taking the numerical curl of the z-component of the magnetic vector potential A_z,

$$B_x = \frac{\partial A_z}{\partial y}, \quad B_y = -\frac{\partial A_z}{\partial x}, \tag{61}$$

where

$$A_z = \begin{cases} A_0(R - r) & \text{if } r \leqslant R, \\ 0 & \text{otherwise}. \end{cases} \tag{62}$$

By using this initialization process, divergence-free magnetic fields are constructed with a maximum value of $\nabla \cdot \mathbf{B}$ in the order of 10^{-16} at the chosen resolution. The parameters in (62) are $A_0 = 10^{-3}$ and a field loop radius $R = 0.3$. This initial condition results in a very high plasma beta $\beta = p/B_\mathrm{p} = 2 \times 10^6$ for the inner region of the field loop. Inside the loop the magnetic field strength is very weak and the flow dynamics is dominated by the gas pressure.

The field loop advection is integrated to a final time $t = 2$. The advection test is found to truly require the full multidimensional MHD approach, i.e., the inclusion of the multidimensional MHD terms (15) and (16) as described in Section 2.1. Since the field loop is advected at an oblique angle to the x-axis of the computational domain, the values of $\partial B_x/\partial x$ and $\partial B_y/\partial y$ are non-zero in general and their roles are crucial in multidimensional MHD flows. These terms, together with the multidimensional MHD terms $\mathbf{A}_{B_x}$ and $\mathbf{A}_{B_y}$, are explicitly included in our data reconstruction–evolution algorithm. During the advection a good numerical scheme should maintain: (a) the circular symmetry of the loop at all time: a numerical scheme that lacks proper numerical dissipation results in spurious oscillations at the loop, breaking the circular symmetry; (b) $B_z = 0$ during the simulation: B_z will grow proportional to $w\nabla \cdot \mathbf{B}\Delta t$ if a numerical scheme does not properly include multidimensional MHD terms.

From the results in Fig. 3, the USM–MEC scheme maintains the circular shape of the loop extremely well to the final time step. The scheme successfully retains the initial circular symmetry and does not develop severe oscillations as indicated in plots (a) and (c). However, in the absence of proper dissipation in the simple electric field averaging scheme in Eq. (47) (i.e.,

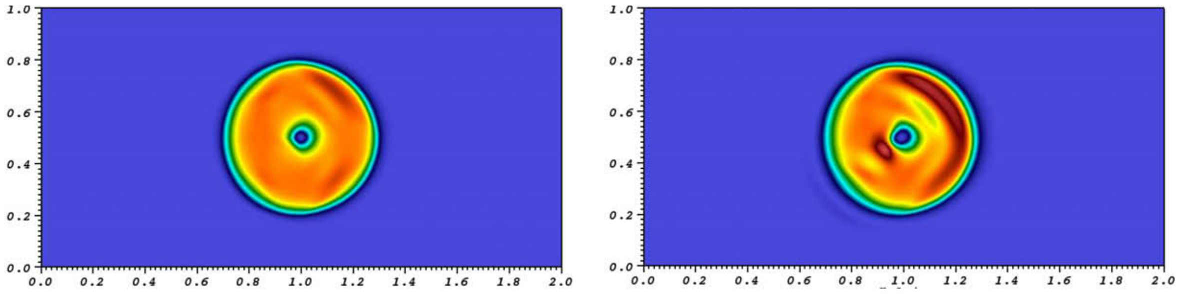

(a) B_p with the MEC at $t = 2$ (b) B_p without the MEC at $t = 2$

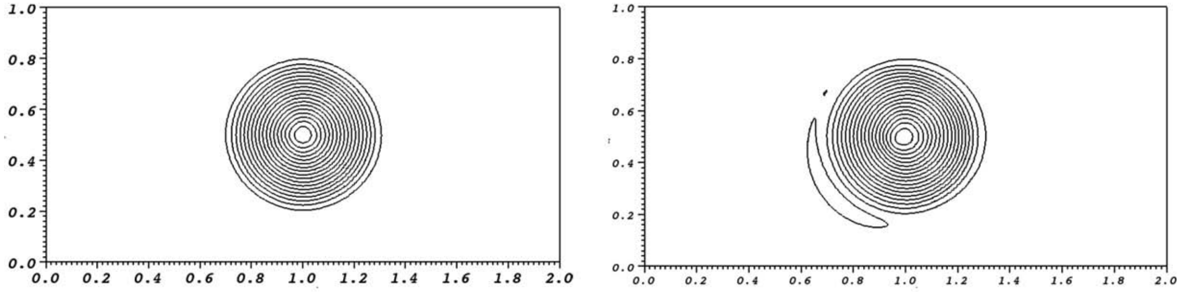

(c) Magnetic field lines with the MEC at $t = 2$ (d) Magnetic field lines without the MEC at $t = 2$

Fig. 3. The field loop advection problem at time $t = 2$ using the Roe Riemann solver. The same color scheme between 2.32×10^{-25} and 7.16×10^{-7} was used for both (a) and (b). 20 contour lines of A_z between -2.16×10^{-6} and 2.7×10^{-4} are shown in (c) and (d).

without using the MEC), the result shows the development of strong numerical oscillations in the field loop as illustrated in plot (b); the associated field lines got distorted and even reconnected forming a big magnetic island in the direction opposite to the advection. Note also that the overall shape of the field lines in (d) has turned oblong, in contrast to (c) where the circular symmetry is preserved well.

Another important issue in the field loop advection problem is to examine the in-plane dynamics for 2D MHD flows. With our choice of the non-zero velocity field $w = 1$ in (60), we consider the B_z component of the induction equation,

$$\frac{\partial B_z}{\partial t} + B_z\frac{\partial u}{\partial x} - B_x\frac{\partial w}{\partial x} - w\frac{\partial B_x}{\partial x} + u\frac{\partial B_z}{\partial x} + B_z\frac{\partial v}{\partial y} - B_y\frac{\partial w}{\partial y} - w\frac{\partial B_y}{\partial y} + v\frac{\partial B_z}{\partial y} = 0. \tag{63}$$

The fourth and eighth terms in Eq. (63) are the multidimensional MHD terms that were taken care of in the data reconstruction–evolution step in the unsplit fashion. The sum of these two is $w\nabla \cdot \mathbf{B} = w(\Delta B_{x,i}/\Delta x + \Delta B_{y,j}/\Delta y)$, and hence if there is any secular growth in the $\nabla \cdot \mathbf{B} = (\Delta B_{x,i}/\Delta x + \Delta B_{y,j}/\Delta y)$ error, it will change the in-plane geometry due to an unphysical growth of B_z with a rate proportional to $w\nabla \cdot \mathbf{B}\Delta t$. For dimensionally-split MHD schemes, this kind of unphysical growth is hard to avoid, since the terms $\Delta B_{x,i}/\Delta x$ and $\Delta B_{y,j}/\Delta y$ are not updated simultaneously.

As the USM–MEC scheme maintains $\nabla \cdot \mathbf{B}$ to machine precision, at time $t = 2$, B_z is of amplitude $\sim 10^{-28}$ and appears featureless with just small scale noise. This result indicates that the scheme does indeed correctly maintain the in-plane geometry without causing an unphysical growth of the out-of-plane field.

5.2. *Circularly polarized Alfvén wave*

In the next test we solve the circularly polarized Alfvén wave and its propagation [40] in order to check the accuracy of the USM–MEC scheme. The Alfvén wave propagates at an oblique angle to the x-axis of the computational domain. This test problem is very useful as a diagnostic of the solution's accuracy because the smooth initial conditions are nonlinear solutions to the problem, and many authors have chosen this problem for testing their scheme's solution accuracy [18,23]. It is also of particular relevance to astrophysical phenomena because the propagation of Alfvén waves in the solar wind is thought to be a possible source for the heating of the solar corona. Hence their accurate modeling is crucial. Further, departures from pure Alfvénic modes are a measure of the interaction of these waves with the solar wind [19,36].

The initial conditions we use are the same as the equivalent test problems described in [16]. A computational domain with a doubly-periodic box $[0, 1/\cos\theta] \times [0, 1/\sin\theta]$ is determined according to the propagation angle θ, and the value we adopt is $\theta = \tan^{-1}(2) \approx 63.44°$. In this configuration, flux terms involving $\partial B_x/\partial x$ and $\partial B_y/\partial y$ are non-zero throughout the domain and their contributions to the solution, especially the magnetic fields, are essential in this problem. For the convergence study we simulated both standing and traveling Alfvén waves.

The grid resolutions used for this problem are $2N \times N$ with $N = 8, 16, 32, 64$, and 128. At time $t = 0$, the density $\rho = 1$ and the gas pressure $p = 0.1$ are set uniformly on the domain with $\gamma = 5/3$. The propagation of the circularly polarized Alfvén wave can be described in a rotated coordinate system $\xi = \mathbf{R}_z(\theta)\mathbf{x}$, so that

$$\mathbf{B} = (B_\xi, B_\eta, B_\zeta) = (1, 0.1\sin 2\pi\xi, 0.1\cos 2\pi\xi). \tag{64}$$

Similarly, the velocity fields are

$$\mathbf{U} = (U_\xi, U_\eta, U_\zeta) = \begin{cases} (0, 0.1\sin 2\pi\xi, 0.1\cos 2\pi\xi) & \text{traveling wave,} \\ (1, 0.1\sin 2\pi\xi, 0.1\cos 2\pi\xi) & \text{standing wave.} \end{cases} \tag{65}$$

In both the standing and traveling cases the Alfvén wave is propagating in the ξ-direction. As suggested in [16] we take numerical curls of the z-component of the magnetic vector potential A_z to assign in-plane magnetic fields B_ξ and B_η,

$$B_\xi = \frac{\partial A_z}{\partial \eta}, \quad B_\eta = -\frac{\partial A_z}{\partial \xi}. \tag{66}$$

From this we integrate $B_\xi, -B_\eta$ with respect to η, ξ, respectively, and sum them to get A_z. We then proceed to take numerical derivatives of A_z with respect to x, y to get B_x and B_y, respectively. The resulting fields are numerically divergence-free in-plane magnetic fields.

Note that in the standing wave case, the propagating Alfvén wave speed, $c_A = |B_\xi|/\sqrt{\rho}$, and the fluid velocity U_ξ are unity, and hence the wave moves with the flow, effectively remaining still in the computational frame.

Fig. 4 shows the numerical errors on a logarithmic scale obtained with different grid resolutions. For each case, the L1 error of the quantities q_k^n at $t = 5$ (i.e., after propagating five wavelengths) is calculated with respect to the initial condition,

$$\delta q_k = \frac{1}{2N^2}\sum_i \sum_j |q_{k,i,j}^n - q_{k,i,j}^0|, \tag{67}$$

by taking a sum over all cell-centered values. The errors are summed over all kth primitive variables p, ρ, u, v, B_x, B_y and we compute the L1 error $||\delta q|| = \sum_{k=1}^6 |\delta q_k|$. Fig. 4 shows a second-order convergence rate of the USM–MEC scheme for the smooth Alfvén wave problem.

The reduction of errors can also be seen in Fig. 4 when using the MEC scheme (labeled as "USM–MEC") as compared to the case without using the MEC (labeled as "USM"), especially in the traveling wave case (labeled as "TW"). This convergence test confirms that the derivative terms in the MEC scheme enhance the solution accuracy by resolving errors from both dissipation and dispersion.

5.3. Orszag–Tang problem

The third test problem is the Orszag–Tang MHD vortex problem [29]. This test problem is widely used in the literature and serves as a good verification test for 2D MHD where nonlinear steepening builds strong discontinuities from smooth initial conditions. The computational domain is $[0, 1] \times [0, 1]$, with a grid resolution of $N \times N$. The initial condition is given by sinusoidal waves,

$$\mathbf{U} = u_0(-\sin \pi y, \sin 2\pi x, 0), \quad \mathbf{B} = B_0(-\sin \pi y, \sin 4\pi x, 0), \tag{68}$$

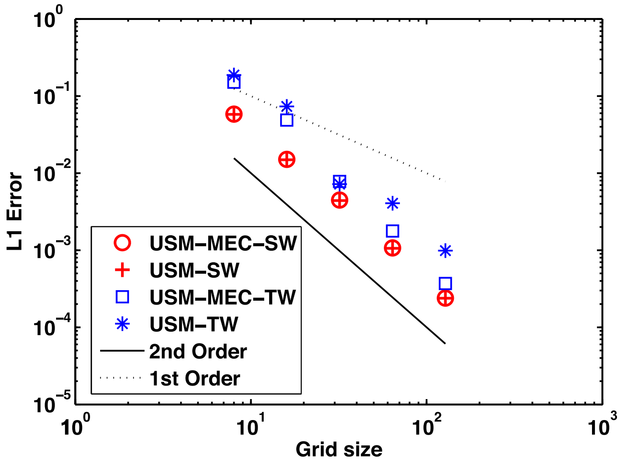

Fig. 4. The circularly polarized Alfvén wave convergence rate for both the standing (labeled as "SW") and traveling (labeled as "TW") wave problems. Two linear rates, labeled as "first-order" and "second-order", are shown as reference rates. The Roe Riemann solver was used for calculations.

where B_0 is chosen so that the ratio of the gas pressure to the rms magnetic pressure is equal to 2γ, with $\gamma = 5/3$. The initial density, speed of sound and u_0 are set to unity, and therefore both the initial pressure and B_0 are set to $1/\gamma$. Periodic boundary conditions are used everywhere. The density contour plots on a 400×400 grid size at times $t = 0.5$ and 1.0 are shown in Fig. 5. The plots show that the initially smooth flow has developed complicated structures involving numerous discontinuities.

5.4. Rotor problem

The rotor problem [2,40] is initialized on a domain of a unit square $[0,1] \times [0,1]$ with non-reflecting boundary conditions on all four sides. The initial condition is given by

$$\rho = \begin{cases} 10 & \text{for } r \leqslant r_0, \\ 1 + 9f(r) & \text{for } r_0 < r < r_1, \\ 1 & \text{for } r \geqslant r_1, \end{cases} \tag{69}$$

$$u = \begin{cases} -f(r)u_0(y - 0.5)/r_0 & \text{for } r \leqslant r_0, \\ -f(r)u_0(y - 0.5)/r & \text{for } r_0 < r < r_1, \\ 0 & \text{for } r \geqslant r_1, \end{cases} \tag{70}$$

$$v = \begin{cases} f(r)u_0(x - 0.5)/r_0 & \text{for } r \leqslant r_0, \\ f(r)u_0(x - 0.5)/r & \text{for } r_0 < r < r_1, \\ 0 & \text{for } r \geqslant r_1, \end{cases} \tag{71}$$

$$p = 1, \quad B_x = \frac{5}{\sqrt{4\pi}}, \quad B_y = 0, \tag{72}$$

where $r_0 = 0.1, r_1 = 0.115, r = \sqrt{(x - 0.5)^2 + (y - 0.5)^2}, w = B_z = 0$, and a taper function $f(r) = (r_1 - r)/(r - r_0)$. The value $\gamma = 1.4$ is used. The initial set-up is occupied by a dense rotating disk at the center of the domain, surrounded by ambient gas at rest with the uniform density and pressure. The rapidly spinning rotor is not in an equilibrium state due to centrifugal forces, and as the rotor spins with the given rotating velocity, the initially uniform magnetic fields in x-direction wind up the rotor. As the magnetic fields wrap around the rotor, torsional Alfvén waves are launched subsequently into the ambient gas until the angular momentum of the rotor is diminished at later times. The circular rotor is progressively compressed into an oval shape by the build-up of the magnetic pressure around the rotor.

Shown in Fig. 6 are the contour plots of the (a) density, (b) gas pressure, (c) Mach number, and (d) magnetic pressure at the final time $t = 0.15$ on a grid resolution 400×400 using the HLLD Riemann solver. For all cases (a)–(d), 30 equally spaced contour lines are plotted. By this final time, we can see in (d) that the Alfvén waves have almost reached the boundary. One of the important features of this rotor test problem is the maintenance of smooth contour profiles in the central part of the Mach number profile [40]. A scheme that produces undershoots in the pressure and correspondingly the sound speed, will result in spurious peaks in the Mach number, especially in the central region. A distortion of the oval contour lines is a signature of a relatively poor performance of a scheme. The USM–MEC scheme shows excellent behavior as illustrated in (c) where such distortions are absent and the rotor possesses smooth contours.

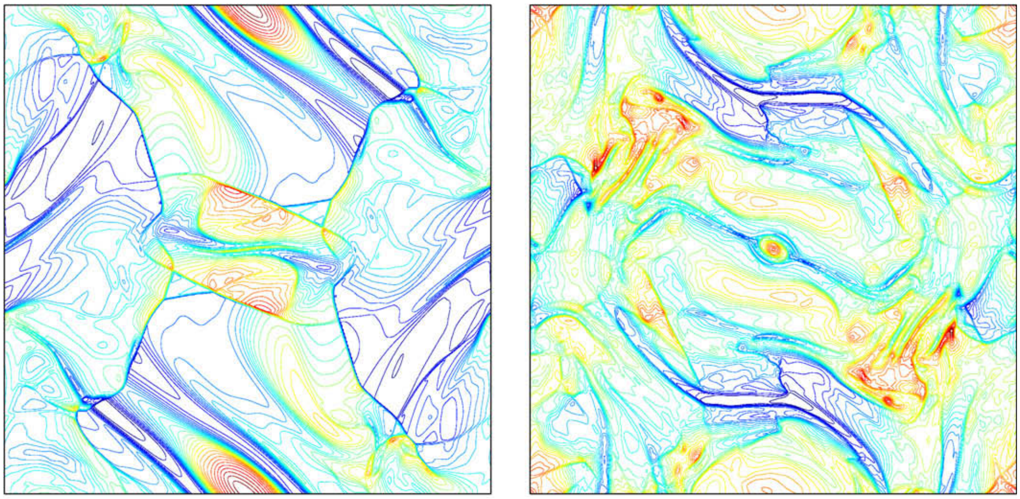

(a) 30 lines between 0.3831 and 2.2414 at $t = 0.5$ (b) 30 lines between 0.1944 and 1.9337 at $t = 1.0$

Fig. 5. The density contour plot of the Orszag–Tang problem at a resolution of 400×400 using the Roe Riemann solver.

For a comparison at the low resolution used in Tóth [40], the Mach number on a 100 × 100 resolution is computed and shown in Fig. 7. In Fig. 20 of [40], seven different Mach number plots were obtained from seven different MHD schemes at the same resolution and compared with each other. Those results can be compared with our plot (b) of Fig. 7. Our low resolution result appears to be among the best presented in [40], indicating that the present scheme is more accurate and reliable than many of the schemes tested by this author.

In the work of Londrillo and Del Zanna [26], a similar rotor problem was presented with minor changes in the flow parameters. While their results appear convincing, the divergence of the magnetic fields as shown reaches values up to the order of 10^{-4} on their 240 × 240 resolution calculation. The USM–MEC scheme, however, keeps this value to the order of 10^{-13} (even with this low resolution of size 100 × 100).

5.5. Cloud and shock interaction

In the next test problem we consider the interaction of a high density cloud with a strong shock wave. This problem, also known as the Dai and Woodward's cloud–shock problem [11], has been studied in several papers [24,40] to test the robust-

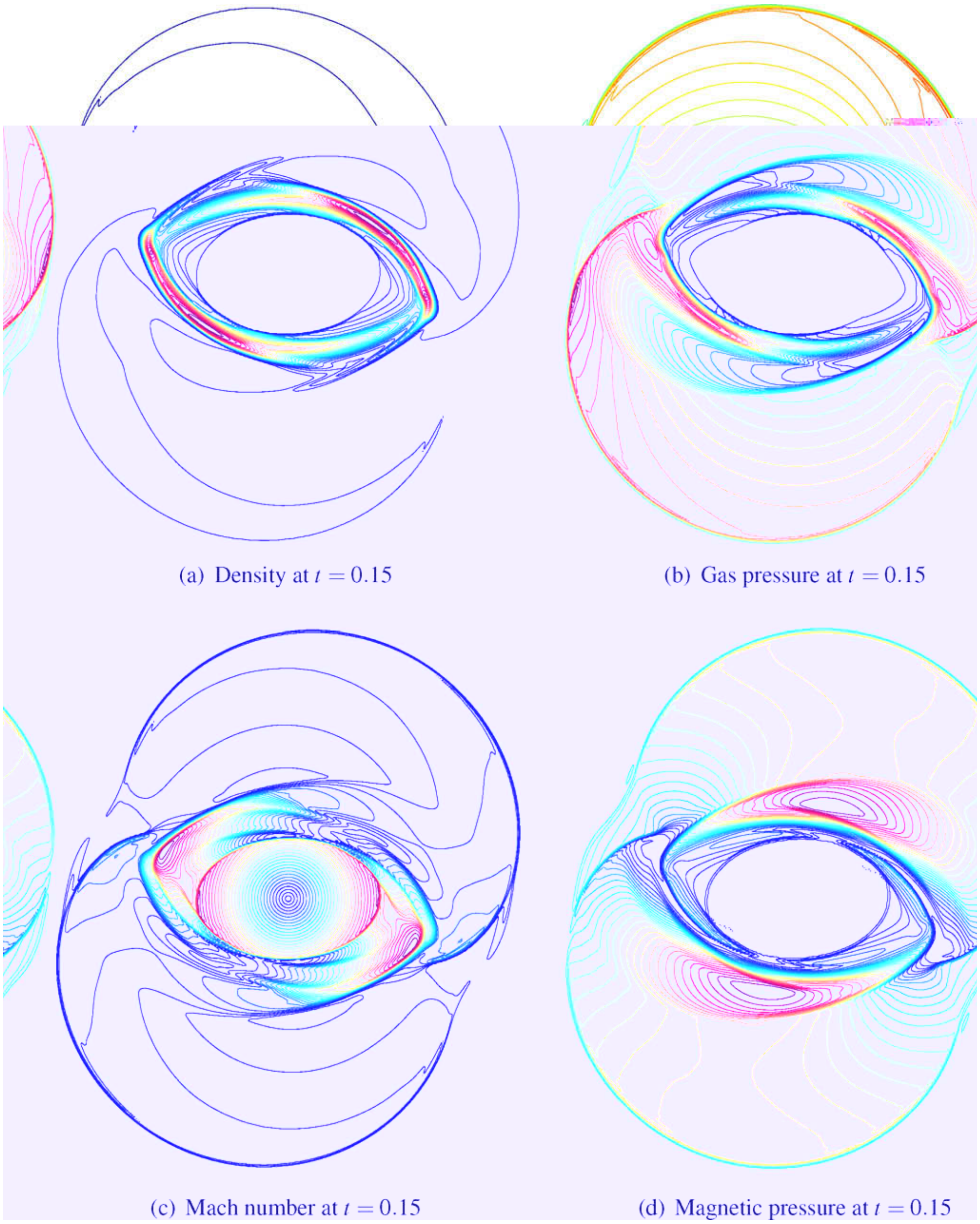

(a) Density at $t = 0.15$

(b) Gas pressure at $t = 0.15$

(c) Mach number at $t = 0.15$

(d) Magnetic pressure at $t = 0.15$

Fig. 6. The rotor problem with a resolution of 400 × 400 using the HLLD Riemann solver. 30 equally spaced contour lines are plotted.

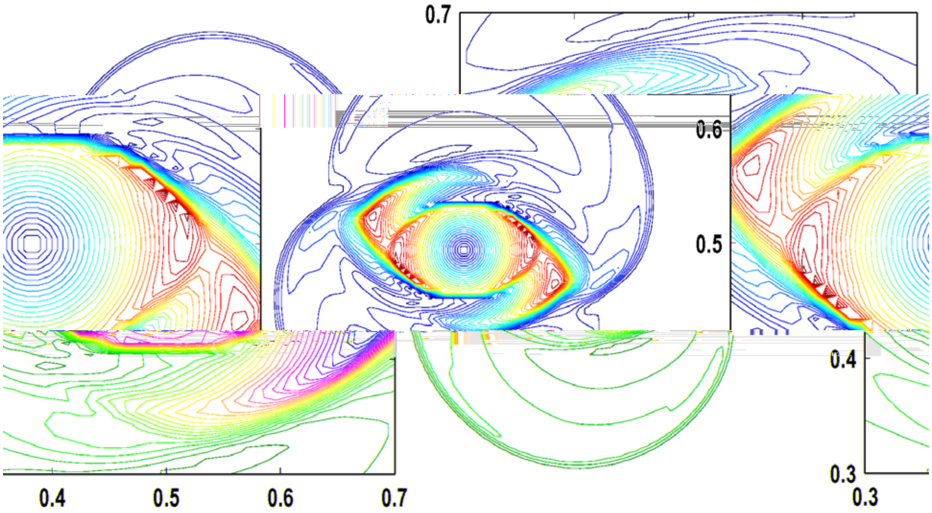

A close up view of the center (a) Mach number at $t = 0.15$ (b)

Fig. 7. The Mach number for the rotor problem on a resolution of 100×100 using the HLLD Riemann solver. 30 equally spaced contour lines are plotted. In (b) the circular shapes of the contour lines are well captured even with this low resolution.

ness of MHD schemes. The challenge for this problem is to demonstrate supersonic flow in the pre-shock and the post-shock regions, as well as the correct physics near the sharp boundary of the cloud.

The same initial condition is adopted as presented in [40]. The flow is solved on a computational domain of size $[0,1] \times [0,1]$ on a uniform $N \times N$ grid. The simulation is carried out to the final time $t = 0.06$ with $N = 400$. The initial discontinuity involves the left and right states along a line $x = 0.6$ parallel to the y-axis, with

$$(\rho, u, v, w, B_x, B_y, B_z, p) = \begin{cases} (3.86859, 0, 0, 0, 0, 2.1826182, -2.1826182, 167.345) & \text{if } x \leqslant 0.6, \\ (1, -11.2536, 0, 0, 0, 0.56418958, 0.56418958, 1) & \text{if } x > 0.6. \end{cases} \tag{73}$$

The high density cloud is located on the right side of the domain, for which its circular shape is defined by $(x-0.8)^2 + (y-0.5)^2 = 0.15^2$. The uniform density $\rho = 10$ and pressure $p = 1$ are fixed in the inner region, and $\gamma = 5/3$. The velocity and the magnetic fields are the same as the surrounding right state plasma values. Supersonic inflow boundary conditions are imposed along the right-most boundary at $x = 1$ and outflow boundary conditions are used for all other boundaries.

As shown in the density plots in Fig. 8, the temporal evolution involves the disruption of the high density cloud by the shock initially located at $x = 0.6$. The red[3] areas indicate the strongly shocked regions and the overall flow features compare well with the results in [24,40]. It was found by Tóth that a dimensionally-split MHD algorithm can easily fail due to unphysical states (e.g., negative pressure or density) produced during the strong interaction of the shock with the cloud even when the rather diffusive Minmod limiter was used. However, in the USM–MEC scheme, using the van Leer's limiter, the final time step is reached successfully without such problems.

5.6. MHD blast wave

The next test case presented is the MHD spherical blast wave problem of Zachary et al. [43]. This problem leads to the formation and propagation of strong MHD discontinuities, relevant to astrophysical phenomena where the magnetic field energy has strong dynamical effects. With a numerical scheme that fails to preserve the divergence-free constraint, unphysical states could be obtained involving negative gas pressure because the background magnetic pressure increases the strength of magnetic monopoles.

This problem was computed in two different flow regimes by considering intermediate and strong magnetic field strengths. The computational domain is a square $[-0.5, 0.5] \times [-0.5, 0.5]$ with a grid of resolution 200×200. The explosion is driven by an over-pressurized circular region at the center of the domain with a radius $r = 0.1$. The initial density is unity everywhere, and the pressure of the ambient gas is 0.1, whereas the pressure of the inner region is 1000. Two different regimes of a uniform magnetic field in the x-direction are studied, with $B_x = 50/\sqrt{4\pi}$ and $100/\sqrt{4\pi}$. These initial conditions result in very low-β ambient plasma states, $\beta = 1 \times 10^{-3}$ and 2.513×10^{-4} respectively. Through these low-β ambient states, the explosion emits almost spherical fast magneto-sonic shocks that propagate with the fastest wave speed. The flow has $\gamma = 1.4$.

---

[3] For interpretation of color in Figs. 3–12, the reader is referred to the web version of this article.

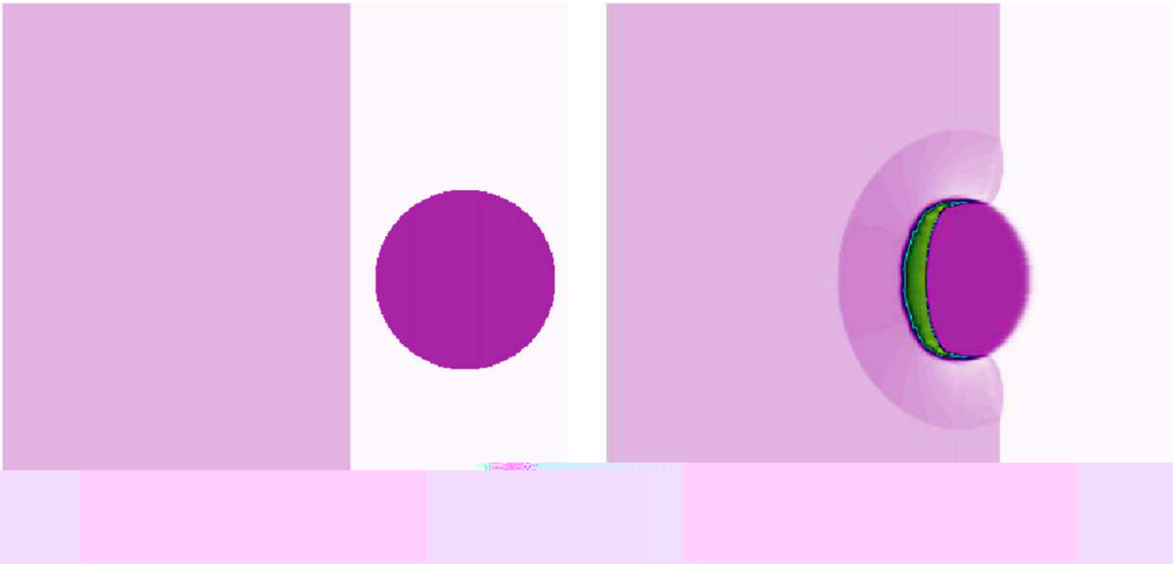

(a) Density at $t = 0.0$ (b) Density at $t = 0.02$

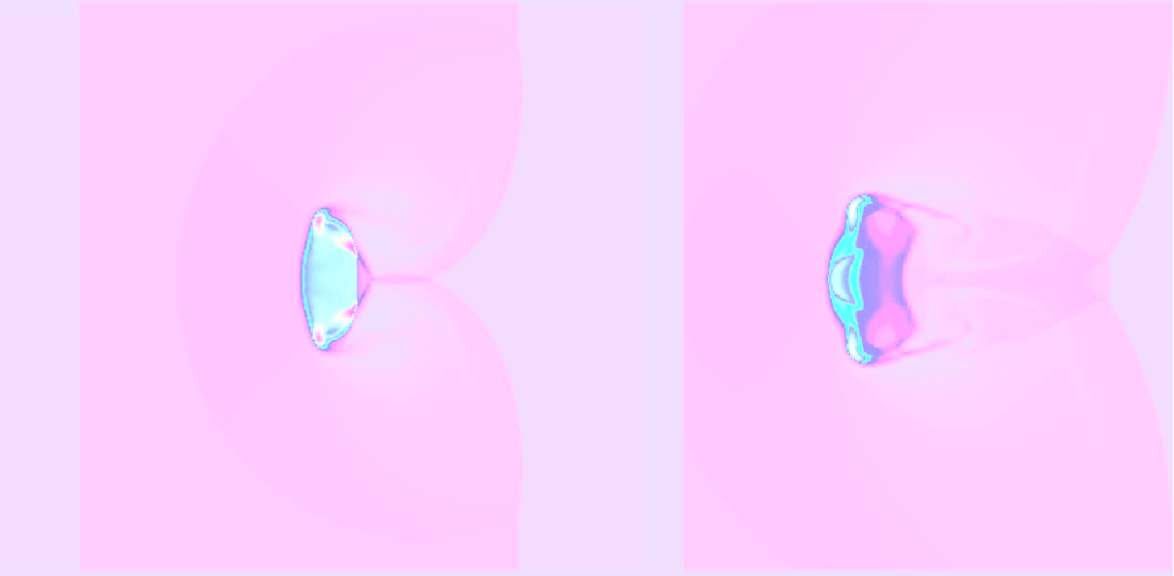

(c) Density at $t = 0.04$ (d) Density at $t = 0.06$

Fig. 8. The MHD interaction between the high density cloud and shock structures resolved on 400 × 400 grid using the HLLD Riemann solver. All plots show a same color scheme ranging between 0.6169 (pink) and 71.82 (red).

The intermediate magnetic field strength case with $B_x = 50/\sqrt{4\pi}$ is illustrated in Fig. 9. An anisotropic explosion behavior is seen because of the existence of the non-zero magnetic field strength in x-direction. With this value of the B_x field, the shock waves still somewhat preserve the spherically symmetric shapes, although the development of the elongated wave structures in the direction parallel to the B_x field are evident.

For the stronger magnetic field case, $B_x = 100/\sqrt{4\pi}$, shown in Fig. 10, the explosion now becomes highly anisotropic. In Fig. 10(b), the displacement of gas in the transverse y-direction is increasingly inhibited and hydrodynamical shocks propagate in both positive and negative x-directions parallel to B_x. It is also evident in (d) that several weak magneto-sonic waves are radiated transverse to x-direction. This process continues until total pressure equilibrium is reached in the central region.

Balsara [4] found that the strong wave propagation oblique to the mesh can cause unphysical negativity in the pressure. Such effects are manifested as distortions of contours especially near the outer boundary where a large and unphysical drop in pressure takes place immediately ahead of the shock. No such excrescence is evident in our calculation.

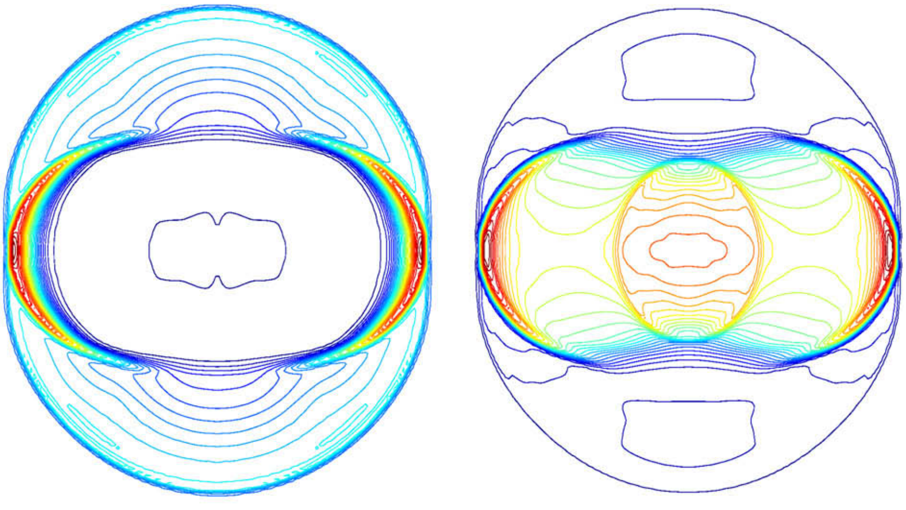

(a) Density at $t = 0.01$ (b) Gas pressure at $t = 0.01$

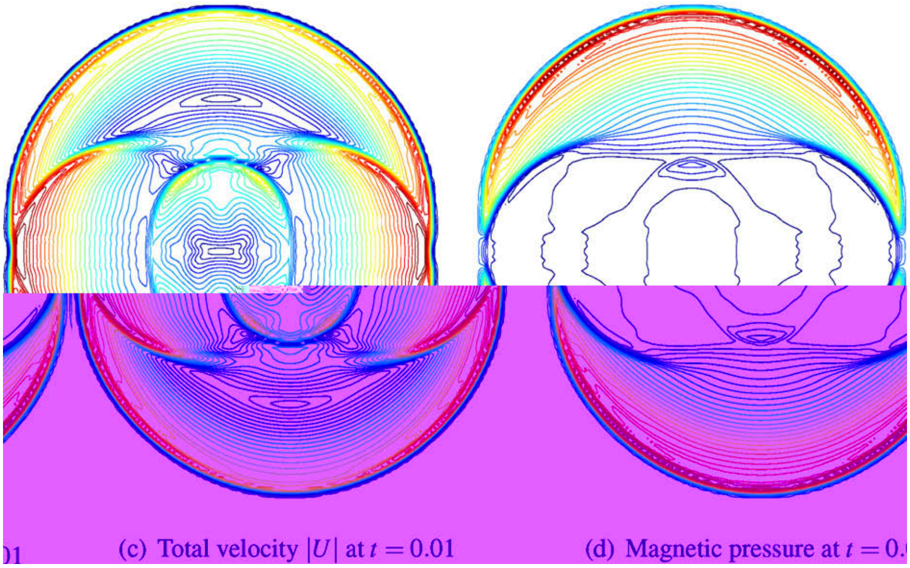

01 (c) Total velocity $|U|$ at $t = 0.01$ (d) Magnetic pressure at $t = 0.$

Fig. 9. Results of the blast problem simulation with $B_x = 50/\sqrt{4\pi}$ using the Roe Riemann solver. 30 contour lines are plotted.

We further consider the possibility of an unphysical drop in pressure by looking at it on a logarithmic scale. It is asserted in [4] the scheme presented there (a modified flux-CT scheme with slope limiters, denoted as the fast TVD limiter and a multidimensional limiter) performs well for this stringent blast problem, and indeed it is stable and able to capture the main features of the flow. However, as published in Fig. 6(b) and (f) of [4], drops in the pressure can be observed particularly in regions where the direction of the strong wave propagation is oblique to the mesh. In their 6(b), with the fast TVD slope limiter employed, distorted profiles at the outer boundary in these regions are evident, while in their Fig. 6(f) these effects are seen to be mitigated but not eliminated with the use of the multidimensional slope limiter. In contrast, as shown in Fig. 11, the USM–MEC scheme displays sharper profiles in these regions at the outer boundary. The modified flux-CT scheme in [4] appears more diffusive than the present scheme and exhibits a narrower bandwidth in the y-direction at the center of the inner blast wave structure. It also appears that the overall wave structures are predicted in more detail with the USM–MEC scheme, while in [4] regions appear featureless with the modified flux-CT scheme using the slope limiters proposed therein, although this could be a plotting artifact of the latter figures. The USM–MEC scheme also produces sharper features in the pre-shock regions in both the negative and positive x-directions, while the figures in Fig. 6(b) and (f) of [4] display more diffuse features.

The test case shows that the USM–MEC scheme does not suffer from observable unphysical effects in strongly shocked cases and continues to maintain sharp features. The results compare quite favorably with those of other MHD schemes which can generate strong distortions of the outer contours (see [22]). For instance, Fig. 19 of [22] shows a contour plot of the den-

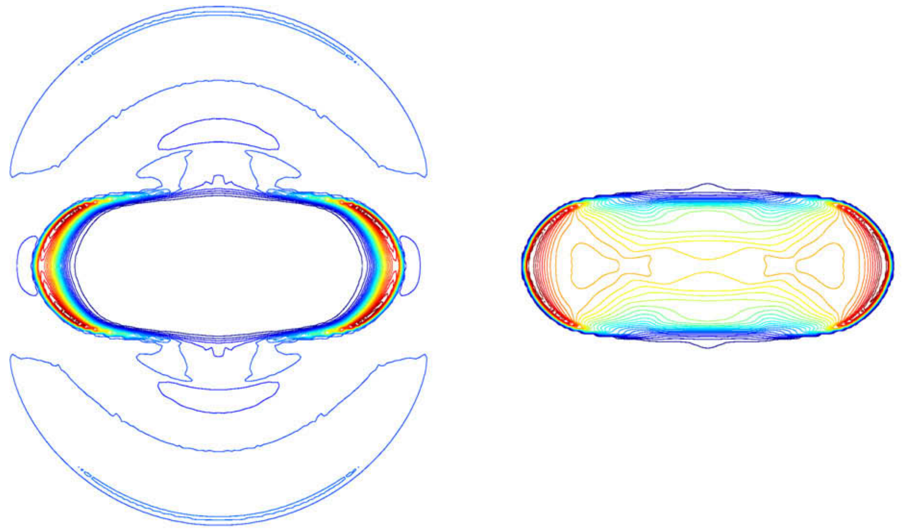

(a) Density at $t = 0.01$ (b) Gas pressure at $t = 0.01$

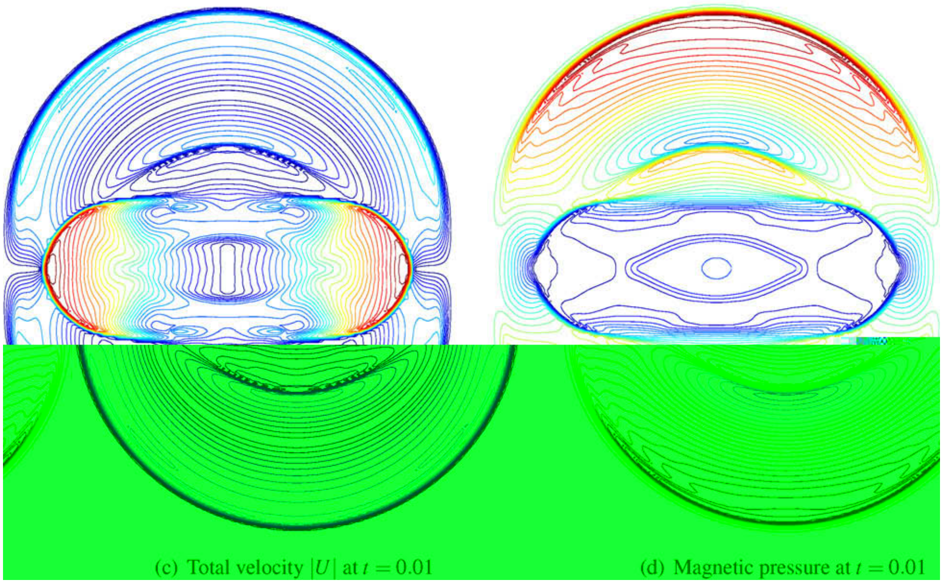

(c) Total velocity $|U|$ at $t = 0.01$ (d) Magnetic pressure at $t = 0.01$

Fig. 10. Results of the blast problem simulation with $B_x = 100/\sqrt{4\pi}$ using the Roe Riemann solver. 30 contour lines are plotted.

sity using the 8-wave scheme of Janhunen [20], where numerous unphysical peaks and distortions are evident. In contrast, smooth contours mark the density field in the USM–MEC calculation shown in Fig. 10(a).

Several other CT-type schemes were tested in [22], including the modified flux-CT of Balsara [4] and upwinding-CT (UTC) schemes of Londrillo and Del Zanna [27]. That study points out that the negativity of the pressure variable could easily be introduced, especially in low-β simulations like this blast problem, and the author found it useful to turn on an energy-fix switch in order to overcome the issue. The situation was found to be more severe in the UTC-based schemes, in that some specific parameters were needed in many cases for successful completion of the calculation. While ameliorating the pressure negativity issue, there still exist other distortions of the fields using those CT-type schemes as indicated in Fig. 17 of [22]. It can also be seen in plots of their so-labeled BS2 and BS3 that there appears to be no qualitative difference between the results when adopting the comparatively newer reconstruction scheme of Balsara [4]. These negativity issue as well as the parameter instability were not found in the USM–MEC scheme, indicating the robustness of our scheme.

5.7. Current sheet and magnetic reconnection

The current sheet test, suggested by Gardiner and Stone [16], concerns the magnetic reconnection process through the presence of two current sheets. This problem is particularly useful in discriminating between algorithms and in demonstrat-

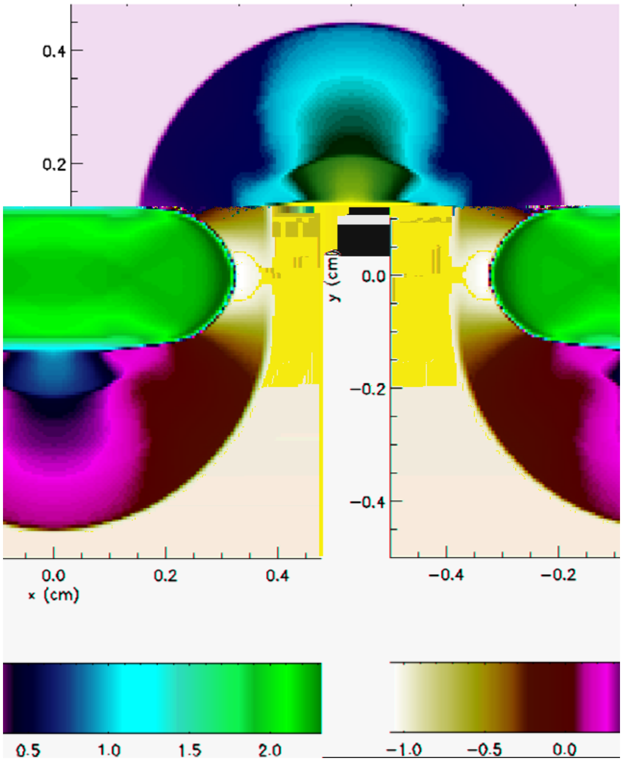

Fig. 11. Shown is $\log_{10} p$ at $t = 0.01$ for the blast problem with $B_x = 100/\sqrt{4\pi}$ using the USM–MEC scheme. The color map is chosen to reveal details.

ing the robustness of integration algorithms. We perform the same test as [16] with the USM–MEC scheme, but consider more stringent flow cases using a set of very low-β values.

Two current sheets are initialized in the computational domain $[-0.5, 0.5] \times [-0.5, 0.5]$ as

$$B_y = \begin{cases} \frac{B_0}{\sqrt{4\pi}} & \text{if } -0.5 \leqslant x < -0.25, \\ -\frac{B_0}{\sqrt{4\pi}} & \text{if } -0.25 \leqslant x \leqslant 0.25, \\ \frac{B_0}{\sqrt{4\pi}} & \text{if } 0.25 < x \leqslant 0.5, \end{cases} \tag{74}$$

where $B_0 = 1$. The other magnetic field components B_x and B_z are set to zero. The problem is resolved on a grid of resolution 400×400 and periodic boundary conditions are applied on all boundaries. The x-component of the velocity is $u = u_0 \sin 2\pi y$ with $u_0 = 0.1$, and all other velocity components are initialized with zero. The density is unity and the gas pressure p is initialized by $p = \beta B_p$. The initial dynamics of the flow is driven by the very strong magnetic forces with our choices of low plasma beta $\beta \ll 1$.

The temporal evolution of the magnetic field lines is shown in Fig. 12 using different values of $\beta = 10^{-3}, 10^{-4}, 10^{-5}$, and 10^{-6}. It has been noted in [38,23] that the algorithms described therein failed to calculate the strongly nonlinear flow dynamics using these set of β values. We find that the USM–MEC scheme does not encounter any instabilities or other failures until a very late time $t = 10$ as illustrated in Fig. 12. With these very low β values, the algorithm should calculate the nonlinear dynamics involving strong compressions and rarefactions, preserving the divergence-free constraint successfully.

As reconnection occurs, it releases strong plasma energy transverse to the field, launching strong magneto-sonic waves. During such reconnection the magnetic energy is converted into thermal energy, which in turn, seeds more reconnections, and thereby a series of magnetic islands are formed along the two current sheets. As seen in Fig. 12 several magnetic islands are observable in different sizes and smaller islands merge into bigger ones with continuous shifts along the current sheets.

5.8. Convergence tests

In this section we present results of convergence tests on the Orszag–Tang (Section 5.3), Rotor (Section 5.4), cloud–shock interaction (Section 5.5), and MHD Blast wave ($B_x = 100/\sqrt{4\pi}$) (Section 5.6) problems. In contrast to the circularly polarized Alfvén wave problem (Section 5.2) where the initial conditions are the exact solutions, these tests do not have any analytical (or exact) solutions. To quantitatively measure errors in these problems we follow the self-convergence relative-error

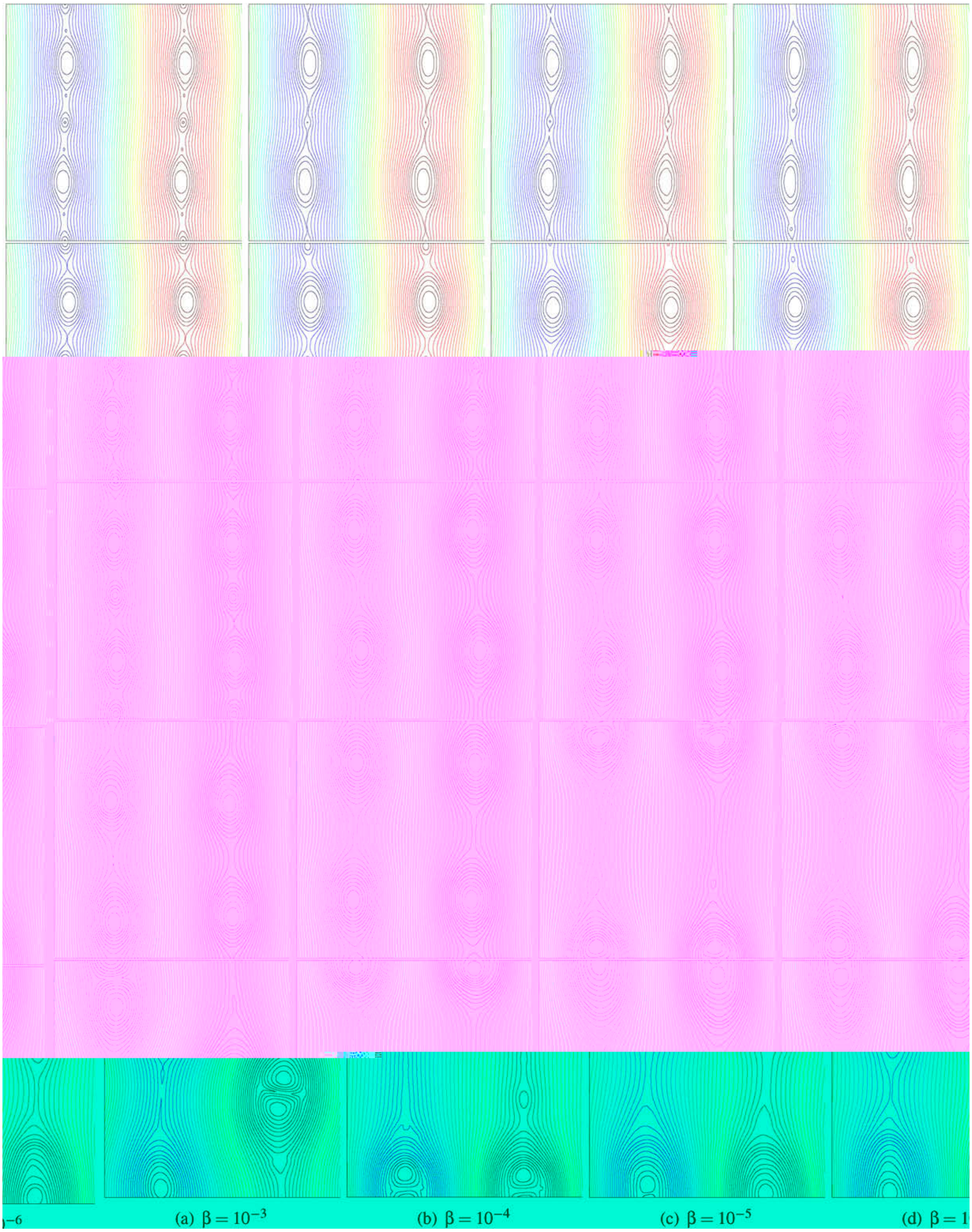

)–6 (a) $\beta = 10^{-3}$ (b) $\beta = 10^{-4}$ (c) $\beta = 10^{-5}$ (d) $\beta = 1$

Fig. 12. Time evolutions of the magnetic field lines for the current sheet problem. Time increases from top to bottom in each column that represents different β values. The sequence of images at times $t = 2, 4, 6, 8, 10$. The formation of the magnetic islands indicates the reconnection process in the simulation. The HLLD Riemann solver was used.

approach as in Tóth [40] to calculate the numerical errors on all the meaningful primitive variables (i.e., p, ρ, u, v, B_x, B_y for all cases and additional w, B_z for the cloud–shock case). For a given variable W the associated error $\delta_{\mathrm{N}}(W)$ is defined as

Table 1
Convergence rates of the four MHD problems using the Roe and HLLD Riemann solvers for solutions at each final time step

	Orszag–Tang at $t = 0.5$			Rotor at $t = 0.15$			Cloud–shock at $t = 0.06$			Blast wave at $t = 0.01$		
Riemann solver	δ_{50}	δ_{100}	δ_{200}	δ_{50}	δ_{100}	δ_{200}	δ_{50}	δ_{100}	δ_{200}	δ_{50}	δ_{100}	δ_{200}
Roe	0.1016	0.0522	0.0199	0.1147	0.0598	0.0250	0.2189	0.1531	0.0805	0.1513	0.0816	0.0364
HLLD	0.0975	0.0498	0.0201	0.1164	0.0592	0.0260	0.2134	0.1496	0.0796	0.1504	0.0807	0.0339

$$\delta_{\mathrm{N}}(W) = \frac{\sum_{j=1}^{N}\sum_{i=1}^{N}|W_{i,j}^{N} - W_{i,j}^{\mathrm{high}}|}{\sum_{j=1}^{N}\sum_{i=1}^{N}|W_{i,j}^{\mathrm{high}}|}, \tag{75}$$

where $W_{i,j}^{\mathrm{high}}$ is the coarsened data at each lower resolution (i.e., $N = 50, 100, 200$) from the high resolution (or reference) data (i.e., $N = 400$). Our reference solutions in all four cases were obtained on 400×400 cells. The averaged error δ_{N} over all primitive variables is then given by

$$\delta_{\mathrm{N}} = \begin{cases} (\delta_{\mathrm{N}}(p) + \delta_{\mathrm{N}}(\rho) + \delta_{\mathrm{N}}(u) + \delta_{\mathrm{N}}(v) + \delta_{\mathrm{N}}(B_x) + \delta_{\mathrm{N}}(B_y))/6, \\ (\delta_{\mathrm{N}}(p) + \delta_{\mathrm{N}}(\rho) + \delta_{\mathrm{N}}(u) + \delta_{\mathrm{N}}(v) + \delta_{\mathrm{N}}(w) + \delta_{\mathrm{N}}(B_x) + \delta_{\mathrm{N}}(B_y) + \delta_{\mathrm{N}}(B_z))/8, \end{cases} \tag{76}$$

where the first is for the Orszag–Tang, Rotor, Blast wave tests and the second is for the cloud–shock interaction test. The results in Table 1 indicate the USM–MEC scheme provides the convergence rate close to 1.0 for the discontinuity dominant flows, while giving the expected second-order accuracy for smoothly varying flows as in the circularly polarized Alfvén wave problem.

6. Conclusion

The USM–MEC scheme has been introduced, developed, and studied in this paper. The method uses characteristic analysis to account for contributions of both normal and transverse MHD fluxes in an unsplit fashion. The scheme handles multidimensional MHD terms consistently using the characteristic method in the data reconstruction–evolution algorithm. Such multidimensional treatment has been ignored in many of the dimensionally-splitting based MHD schemes. Our new approach involves physical considerations that multidimensional MHD schemes should manifest. In particular, such multidimensional considerations eliminate unphysical secular growth that would cause deviations from the in-plane dynamical evolution. To ascertain the correct in-plane dynamics, the 2D MHD problem of field loop advection was tested. Spurious numerical errors proportional to $\nabla \cdot \mathbf{B}$ would affect the growth of B_z, and ultimately alter the in-plane dynamics of the problem. These errors were found to be absent in the current scheme. The presented data reconstruction–evolution method not only resolves the issue but is also significantly advantageous in extending the 2D algorithm to a 3D implementation in a straightforward way, allowing a wide range of CFL stability limit, e.g., less than 1.0.

We also present the new MEC scheme that appears to improve the solution accuracy of similar schemes (e.g., the flux-CT scheme of [2]) by incorporating more directional considerations of the high-order Godunov fluxes obtained from the duality relationship in the flux-CT scheme. The high-order terms introduced in the MEC scheme accounts for proper amounts of numerical dissipation that manifests correct physical evolutions of MHD flows in the stringent set of numerical simulations given in our test suites.

The results of several test problems give considerable confidence in our scheme for use as a robust and reliable second-order MHD algorithm. The full USM–MEC scheme preserves the divergence-free constraint extremely well without any evidence of numerical instabilities or accumulation of unphysical errors. As verification, the suite of test problems presented in this study include several stringent setups that stress various features of MHD algorithms. The scheme has been thoroughly tested and has been shown to perform very well, providing confidence in correctly simulating a wide range of magnetohydrodynamic physical phenomena (i.e., $\beta \approx 10^{\pm 6}$).

This paper has detailed the core algorithmic features of the USM–MEC scheme, laying down the important multidimensional aspects, and subjecting it to a series of tests. The overall USM–MEC scheme utilizes the compact grid stencil arrangements for the second-order accuracy on each local cell, allowing a very efficient and easy implementation on hierarchical AMR grid structures. In subsequent publications we will present extensions of this scheme that support parallel adaptive mesh refinement (early parallel results were reported in [21]) and an implementation in 3D.

The scheme presented here for 2D as well as a full 3D implementation on both uniform and AMR grids have been integrated and tested in the freely available FLASH3 release of the University of Chicago ASC FLASH Center [15].

Acknowledgments

This work has been supported in part by National Science Foundation ITR Grant DMS-0219282. The FLASH code has been developed by the DOE-supported ASC/Alliance Center for Astrophysical Thermonuclear Flashes at the University of Chicago. This work is supported by the US Department of Energy under Grant No. B523820 to the Center for Astrophysical Thermonuclear Flashes at the University of Chicago. The first author gratefully acknowledge the FLASH code group for help and for supporting the current work. The authors would like to thank Dr. James Stone at the Princeton University and Dr. Timur Linde, previously at the FLASH center and now in industry, for useful discussions and comments on an early work of this paper. We also acknowledge useful discussions with Dr. Robert Fisher at the FLASH center, University of Chicago. We also thank Dr. Phil Colella at the LLBL and anonymous referees for helpful suggestions and comments. The authors especially thank Dr. Kevin Olson at the Drexel University for helpful support during the course of this work.

References

[1] D.S. Balsara, Total variation diminishing scheme for adiabatic and isothermal magnetohydrodynamics, Astrophys. J. Suppl. 116 (1998) 133–153.
[2] D.S. Balsara, D.S. Spicer, A staggered mesh algorithm using high order Godunov fluxes to ensure solenoidal magnetic fields in magnetohydrodynamics simulation, J. Comput. Phys. 149 (1999) 270–292.
[3] D.S. Balsara, Divergence-free adaptive mesh refinement for magnetohydrodynamics, J. Comput. Phys. 174 (2001) 614–648.
[4] D.S. Balsara, Second-order-accurate schemes for magnetohydrodynamics with divergence-free reconstruction, Astrophys. J. Suppl. 151 (2004) 149–184.
[5] D.S. Balsara, D. Kim, An intercomparison between divergence-cleaning and staggered mesh formulations for numerical magnetohydrodynamics, Astrophys. J. 602 (2004) 1079–1090.
[6] S.H. Brecht, J.G. Lyon, J.A. Fedder, K. Hain, A time-dependent three-dimensional simulation of the earth's magnetosphere: reconnection events, Geophys. Res. Lett. 8 (1981) 397.
[7] M. Brio, C.C. Wu, An upwind differencing scheme for the equations of ideal magnetohydrodynamics, J. Comput. Phys. 75 (1988) 400–422.
[8] P. Colella, Multidimensional upwind methods for hyperbolic conservation laws, J. Comput. Phys. 87 (1990) 171–200.
[9] R.K. Crockett, P. Colella, R.T. Fisher, R.I. Klein, C.F. McKee, An unsplit, cell-centered godunov method for ideal MHD, J. Comput. Phys. 203 (2005) 422–448.
[10] W. Dai, P. Woodward, An approximate Riemann solver for ideal magnetohydrodynamics, J. Comput. Phys. 111 (1994) 354–372.
[11] W. Dai, P. Woodward, A simple finite difference scheme for multidimensional magnetohydrodynamics, J. Comput. Phys. 142 (1998) 331–369.
[12] A. Dedner, F. Kemm, D. Kröner, C.D. Munz, T. Schnitzer, M. Wesenberg, Hyperbolic divergence cleaning for the MHD equations, J. Comput. Phys. 175 (2002) 645–673.
[13] C.R. DeVore, Flux corrected transport techniques for multidimensional compressible magnetohydrodynamics, J. Comput. Phys. 92 (1991) 142–160.
[14] C.R. Evans, J.F. Hawley, Simulation of magnetohydrodynamic flows: a constrained transport method, Astrophys. J. 332 (1988) 659–677.
[15] FLASH, 2008, <http://flash.uchicago.edu>.
[16] T. Gardiner, J. Stone, An unsplit Godunov method for ideal MHD via constrained transport, J. Comput. Phys. 205 (2005) 509–539.
[17] T. Gardiner, J. Stone, An unsplit Godunov method for ideal MHD via constrained transport in three dimensions, J. Comput. Phys. 227 (2008) 4123–4141.
[18] J. Stone, T. Gardiner, P. Teuben, J. Hawley, J. Simon, Athena: a new code for astrophysical MHD, 2 April 2008. Available from: <arXiv:0804.0402v1> [astro-ph] .
[19] M.L. Goldstein, D.A. Roberts, A.E. Deane, S. Ghosh, Numerical simulation of Alfvénic turbulence in the solar wind, J. Geophys. Res. 104 (A7) (1999) 14437–14451.
[20] P. Janhunen, A positive conservative method for magnetohydrodynamics based on HLL and Roe methods, J. Comput. Phys. 160 (2000) 649–661.
[21] D. Lee, A. Deane, A parallel unsplit staggered mesh algorithm for magnetohydrodynamics, in: A. Deane et al. (Eds.), Parallel Computational Fluid Dynamics, Elsevier, 2006.
[22] S. Li, Note on Upwinding Constrained Transport Method for Ideal Magnetohydrodynamics, Los Alamos Report, LA-UR-03-8925, 2003.
[23] S. Li, High order central scheme on overlapping cells for magneto-hydrodynamic flows with an without constrained transport method, J. Comput. Phys. 227 (2008) 7368–7393.
[24] S. Li, H. Li, A modern code for magneto-hydrodynamics or hydrodynamics equations, Los Alamos Report, LA-UR-03-8925, 2003.
[25] Y. Liu, C.W. Shu, E. Tadmor, M. Zhang, Non-oscillatory hierarchical reconstruction for central and finite-volume schemes, Commun. Comput. Phys. 2 (2007) 933–963.
[26] P. Londrillo, L. Del Zanna, High order upwind schemes for multidimensional magnetohydrodynamics, Astrophys. J. 530 (2000) 508–524.
[27] P. Londrillo, L. Del Zanna, On the divergence-free condition in Godunov-type schemes for ideal magnetohydrodynamics: the upwind constrained transport method, J. Comput. Phys. 195 (2004) 14–48.
[28] T. Miyoshi, K. Kusano, A multi-state HLL approximate Riemann solver for ideal magnetohydrodynamics, J. Comput. Phys. 208 (2005) 315–344.
[29] A. Orszag, C.M. Tang, Small-scale structure of two-dimensional magnetohydrodynamics turbulence, J. Fluid Mech. 90 (1979) 129–143.
[30] U. Pen, P. Arras, S. Wong, A free, fast, simple and efficient TVD MHD code, Astrophys. J. Suppl. 149 (2003) 447–455.
[31] K.G. Powell, A riemann solver for ideal MHD: that works in more than one dimension, ICASE Report, 94–24, Langely, VA, 1994.
[32] K.G. Powell, P.L. Roe, T.J. Linde, T.I. Gombosi, D.L. De Zeeuw, A solution-adaptive upwind scheme for ideal magnetohydrodynamics, J. Comput. Phys. 154 (1999) 284–309.
[33] P.L. Roe, Approximate Riemann solvers, parameter vectors, and difference schemes, J. Comput. Phys. 43 (1981) 357–372.
[34] D. Ryu, T.W. Jones, Numerical magnetohydrodynamics in astrophysics: algorithm and tests for one-dimensional flow, Astrophys. J. 442 (1995) 228–258.
[35] D. Ryu, F. Miniati, T.W. Jones, A. Frank, A divergence-free upwind code for multidimensional magnetohydrodynamic flow, Astrophys. J. 509 (1999) 244–255.
[36] M.S. Ruderman, M.L. Goldstein, D.A. Roberts, A.E. Deane, L. Ofman, Alfvén wave phase mixing driven by velocity shear in two-dimensional open magnetic configurations, J. Geophys. Res. 104 (A8) (1999) 17057–17068.
[37] J. Saltzman, An unsplit 3D upwind method for hyperbolic conservation laws, J. Comput. Phys. 115 (1994) 153–168.
[38] J. Stone, The Athena Test Suite, <http://www.astro.princeton.edu/~jstone>.
[39] E.F. Toro, Riemann Solvers and Numerical Methods for Fluid Dynamics, A Practical Introduction, Springer, 1997.
[40] G. Tóth, The $\nabla \cdot B = 0$ constraint in shock-capturing magnetohydrodynamics codes, J. Comput. Phys. 161 (2000) 605–656.
[41] B. van Leer, Towards the ultimate conservative difference scheme. V. A second-order Sequel to Godunov's method, J. Comput. Phys. 32 (1979) 101–136.
[42] K.S. Yee, Numerical solution of initial boundary value problems involving Maxwell's equations in isotropic media, IEEE Trans. Antenna Propag. AP-14 (1966) 302–307.
[43] A. Zachary, A. Malagoli, P. Colella, A higher-order Godunov method for multidimensional ideal magnetohydrodynamics, SIAM J. Sci. Comput. 15 (1994) 263–284.